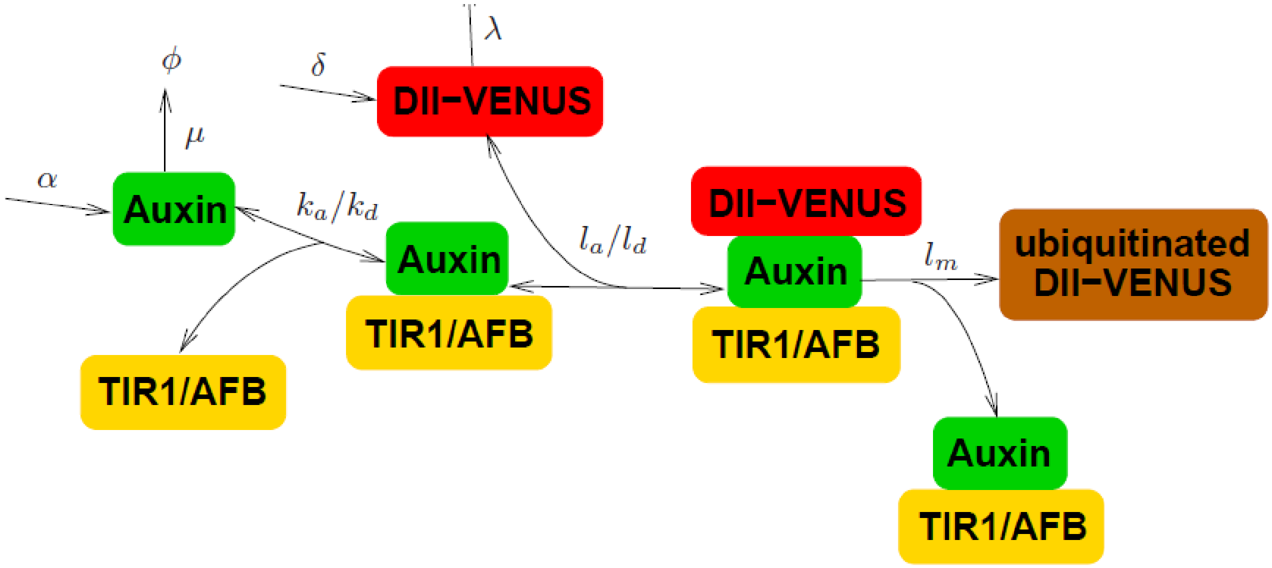

Supplemental Figure 1. The network of interactions that leads to auxin-mediated degradation of DII-VENUS.

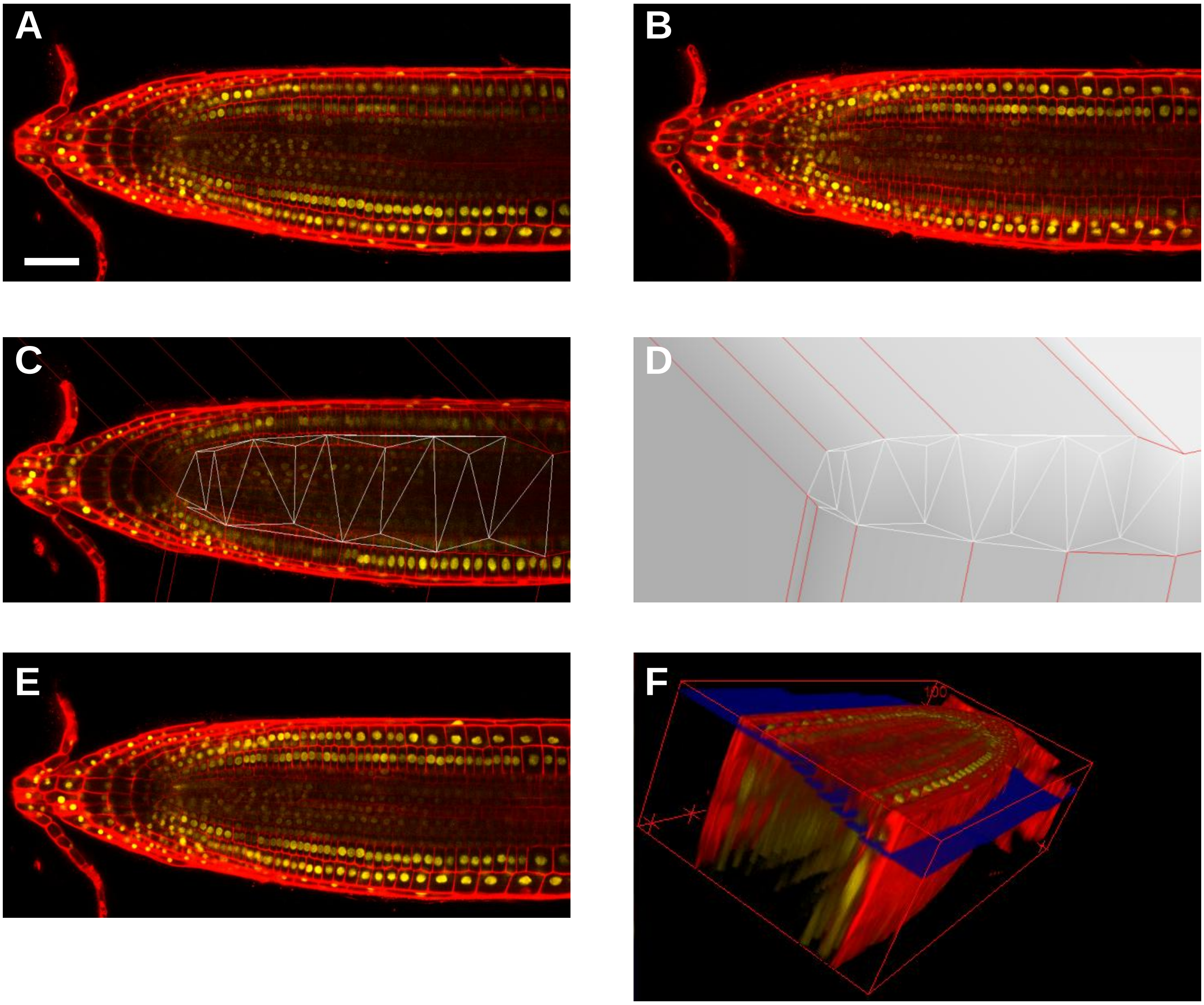

Supplemental Figure 2. Constructing a 2D plane from a confocal image stack, using SurfaceProject. **(A)** Sample plane 26. **(B)** Sample plane 31. **(C)** User-specified triangulation of the surface. **(D)** Depth map. **(E)** Output 2D interpolated slice. **(F)** 3D measuring plane (blue) through the stack. Scale bar: $50\,\mu\text{m}$.

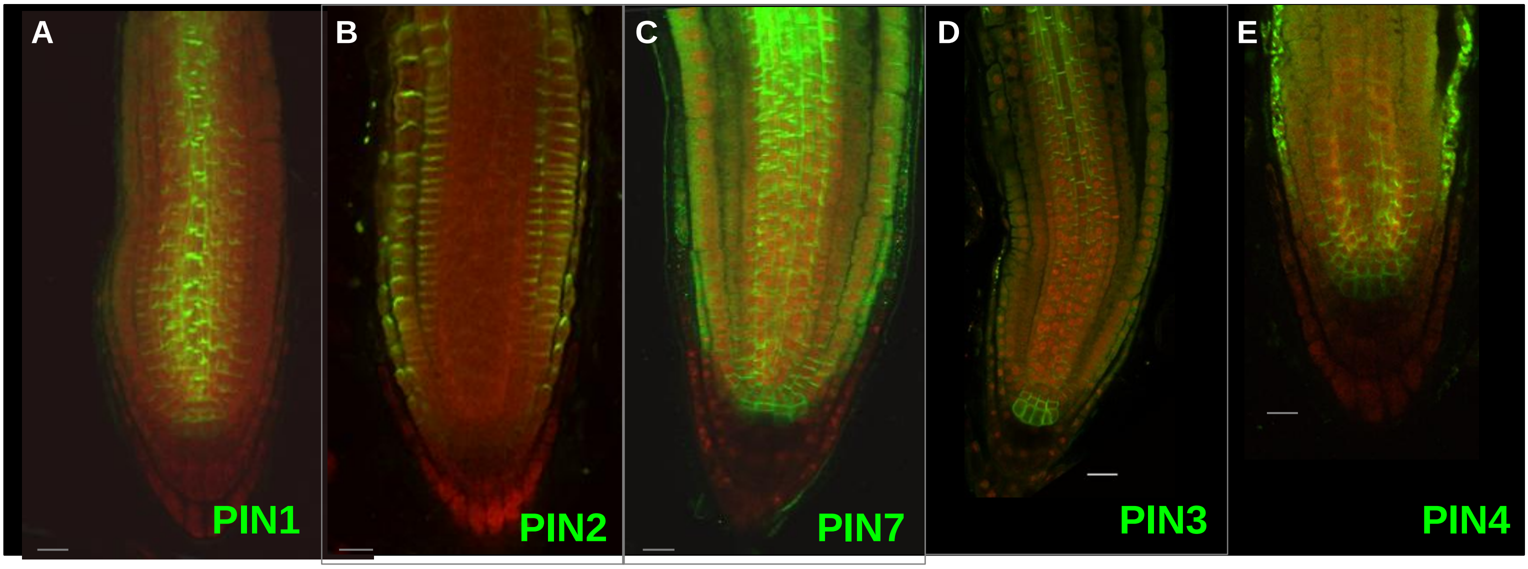

Supplemental Figure 3. In situ immunodetection of PIN proteins (green) in the Arabidopsis root tip, counter stained with propidium iodide (red). Sheep anti PIN1 (A), PIN2 (B), PIN7 (C), PIN3 (D) and PIN4 (E) antibodies (1:200 dilution) were used for immunodetection of these proteins and visualised using Alexafluor488 coupled anti sheep secondary antibody (1:200 dilution). Scale bars: 10 μm.

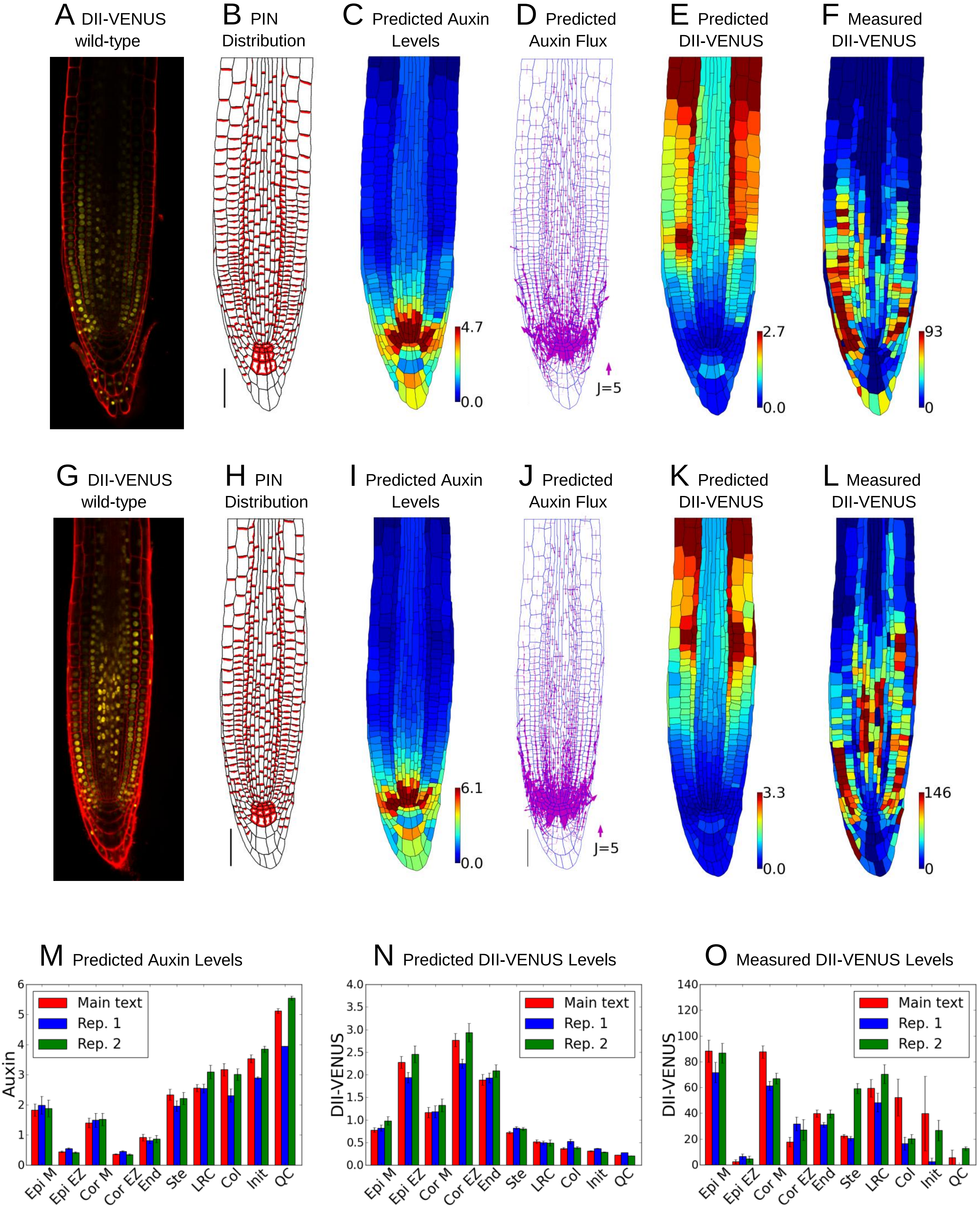
A DII-VENUS wild-type
B PIN Distribution
C Predicted Auxin Levels
4.7
0.0
D Predicted Auxin Flux
J=5
E Predicted DII-VENUS
2.7
0.0
F Measured DII-VENUS
93
0
G DII-VENUS wild-type
H PIN Distribution
I Predicted Auxin Levels
6.1
0.0
J Predicted Auxin Flux
J=5
K Predicted DII-VENUS
3.3
0.0
L Measured DII-VENUS
146
0
M Predicted Auxin Levels
Auxin
0
1
2
3
4
5
6
Main text
Rep. 1
Rep. 2
Epi M
Epi EZ
Cor M
Cor EZ
End
Ste
LRC
Col
Init
QC
N Predicted DII-VENUS Levels
DII-VENUS
0.0
0.5
1.0
1.5
2.0
2.5
3.0
3.5
4.0
Main text
Rep. 1
Rep. 2
Epi M
Epi EZ
Cor M
Cor EZ
End
Ste
LRC
Col
Init
QC
O Measured DII-VENUS Levels
DII-VENUS
0
20
40
60
80
100
120
140
Main text
Rep. 1
Rep. 2
Epi M
Epi EZ
Cor M
Cor EZ
End
Ste
LRC
Col
Init
QC

Supplemental Figure 4. Replicates of results for the wild-type root tip considering efflux-carrier-mediated transport only (i.e. with no influx carriers present). (Replicates of results shown in Figure 1, main text).
(A-F) Replicate 1. **(G-L)** Replicate 2. **(A,G)** Confocal image showing DII-VENUS (yellow) and cell geometries (red) within an *Arabidopsis* root tip (stained with propidium iodide). **(B,H)** Prescribed PIN distribution. **(C,I)** Predicted auxin distribution. **(D,J)** Predicted auxin flux (with arrow width scaling with flux). **(E,K)** Predicted DII-VENUS distribution. **(F,L)** Measured DII-VENUS levels extracted from the confocal images in (A,G). **(M)** Mean predicted auxin concentrations in the different cell types predicted for the three replicates. **(N)** Mean predicted DII-VENUS concentrations in the different cell types predicted for the three replicates. **(O)** Mean measured DII-VENUS levels in the different cell types for the three replicates. In (M-O), error bars show one standard error; Epi=epidermis, Cor= cortex, End=endodermis, Ste= stele, Col=columella, Init=columella initials, M= meristem, EZ=elongation zone; Figure 1A shows the location of the different cell types, and Supplemental Table 1 lists the number of cells in each category. Scale bars: 50 μm.

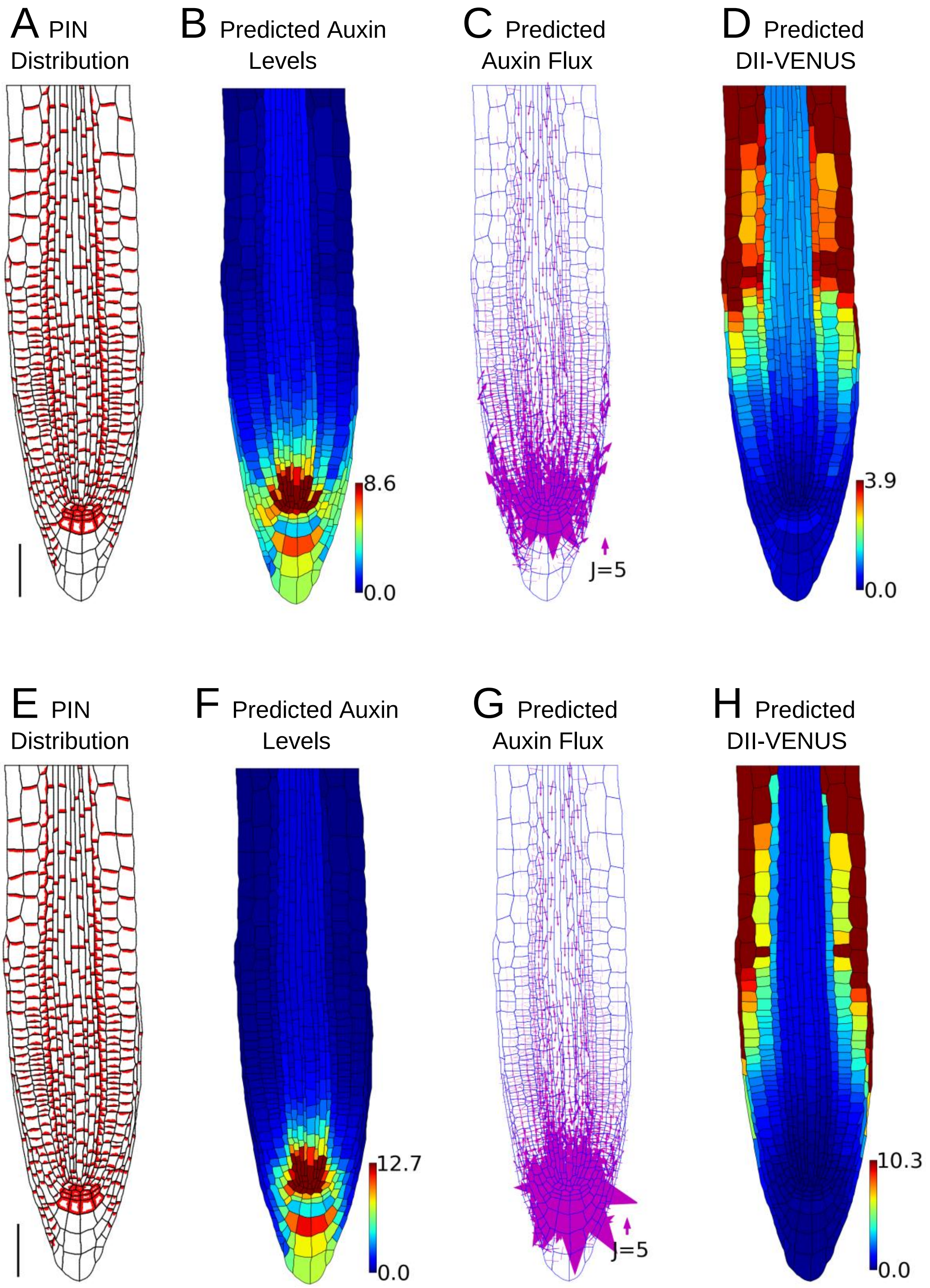

Supplemental Figure 5. Effect of periclinal PINs on the predicted distributions and fluxes with efflux-carrier-mediated transport only (i.e. with no influx carriers present).
(A-D) With inner periclinal PINs on epidermal cell membranes. **(E-H)** With inner periclinal PINs on epidermal, cortical and LRC cell membranes. **(A,E)** Prescribed PIN distribution. **(B,F)** Predicted auxin distribution. **(C,G)** Predicted auxin flux (with arrow width scaling with flux). **(D,H)** Predicted DII-VENUS distribution. Scale bars: 50 μm.

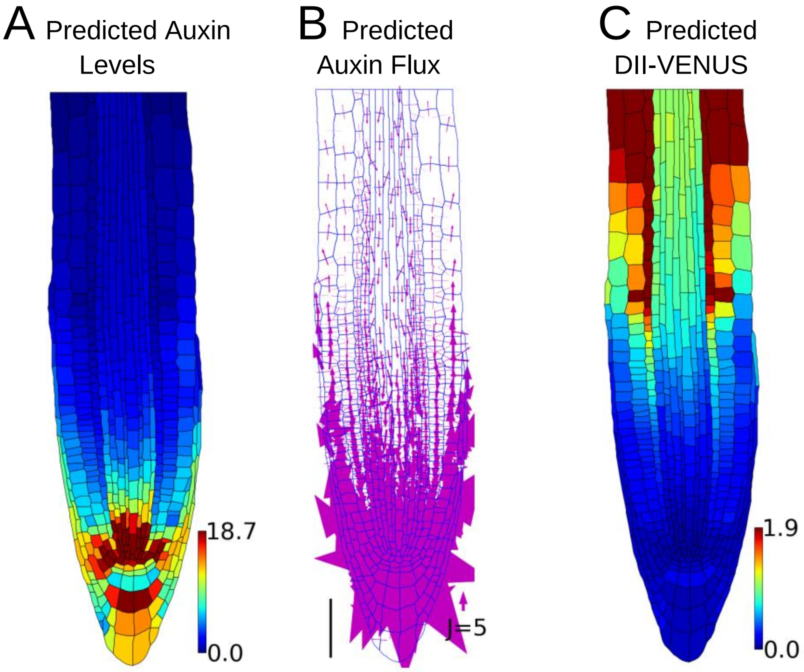

Supplemental Figure 6. Effect of omitting auxin synthesis and degradation on the predicted distributions and fluxes with efflux-carrier-mediated transport only (i.e. with no influx carriers present). **(A)** Predicted auxin distribution. **(B)** Predicted auxin flux (with arrow width scaling with flux). **(C)** Predicted DII-VENUS distribution.

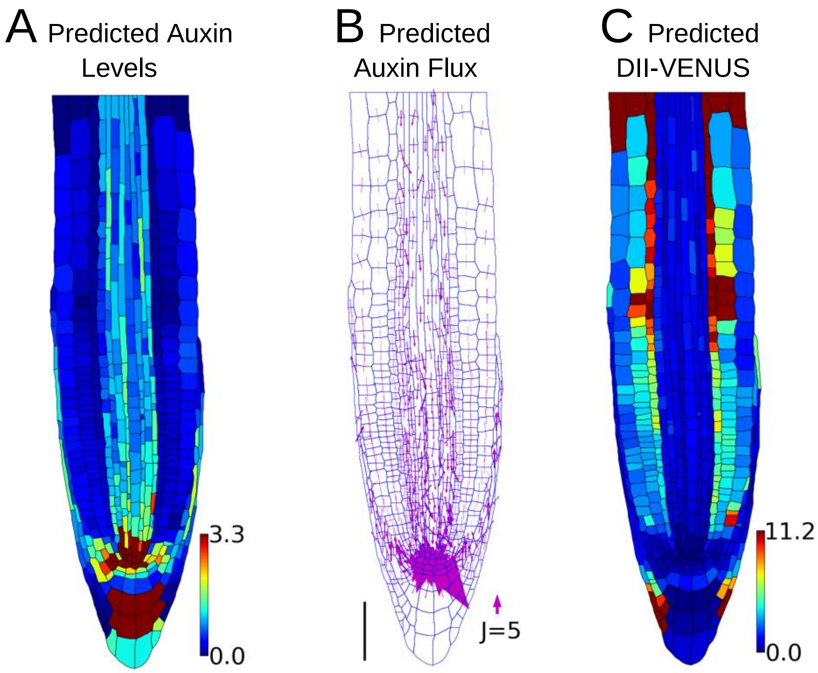

Supplemental Figure 7. Effect of omitting non-polar efflux (as mediated by non-polar PINs and/or ABCBs) on the predicted distributions and fluxes with efflux-carrier-mediated transport only (i.e. with no influx carriers present).

(A) Predicted auxin distribution.

(B) Predicted auxin flux (with arrow width scaling with flux).

(C) Predicted DII-VENUS distribution. Scale bars: 50 μm.

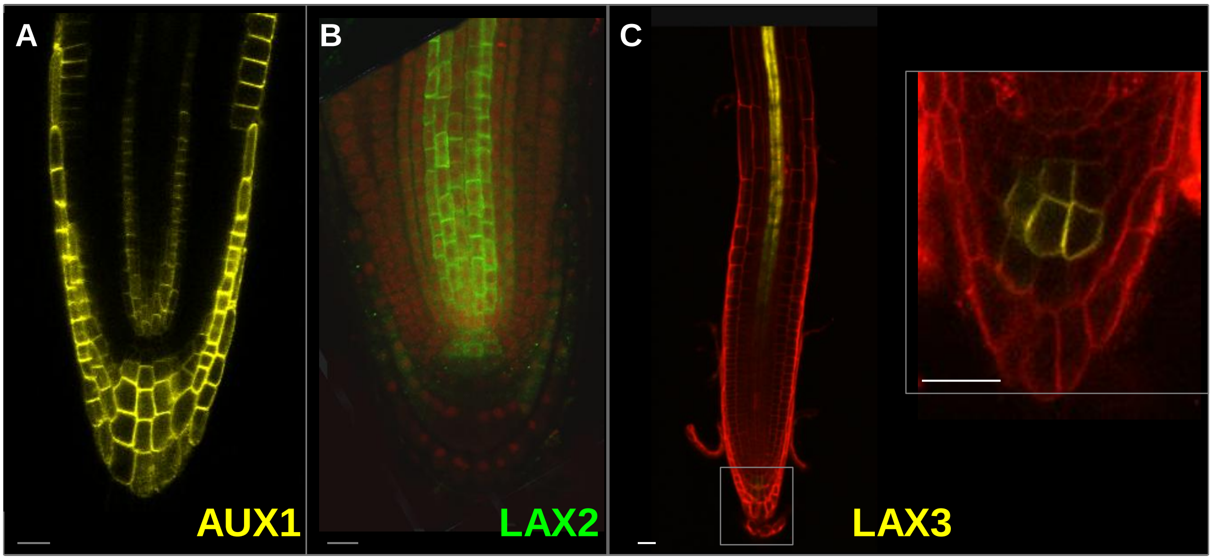

Supplemental Figure 8. Expression patterns of AUX/LAX auxin transporters in Arabidopsis root tip. **(A)** Confocal imaging of seedlings expressing AUX1-YFP. **(B)** In situ immunodetection of LAX2 (green) in the primary roots using affinity purified LAX2 antibody (1:100 dilution) and Oregon Green coupled anti rabbit secondary antibody (1:200 dilution). Roots were counter stained with propidium iodide (red). **(C)** Confocal analysis of seedlings expressing LAX3-YFP (yellow) in the primary roots counter stained with propidium iodide (red). Inset: Higher magnification image of LAX3-YFP expression in columella cells. Scale bars: 10 μm (A,B); 20 μm (C and inset).

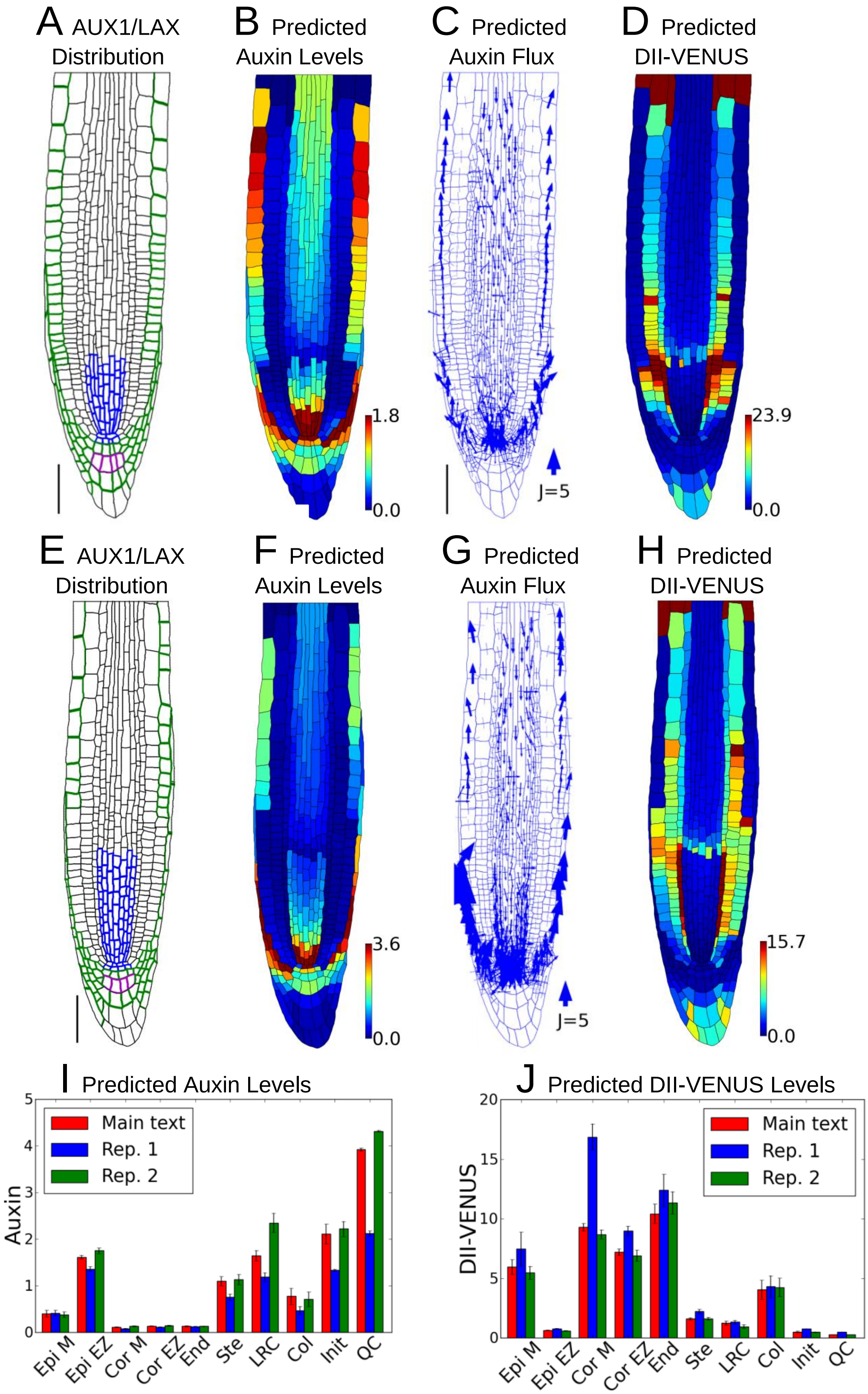

Supplemental Figure 9. Replicates of predictions for the wild-type plant root with auxin transport mediated by both efflux and influx carriers. (Replicates of results shown in Figure 2, main text.) **(A-D)** Replicate 1. **(E-H)** Replicate 2. **(A,E)** Prescribed distributions of AUX1 (green and purple), LAX2 (blue) and LAX3 (purple). **(B,F)** Predicted auxin distribution. **(C,G)** Predicted auxin flux (with arrow width scaling with flux). **(D,H)** Predicted DII-VENUS distribution. **(I)** Mean predicted auxin concentrations in the different cell types for the three replicates. **(J)** Mean predicted DII-VENUS concentrations in the different cell types for the three replicates. Scale bars: 50 μm.

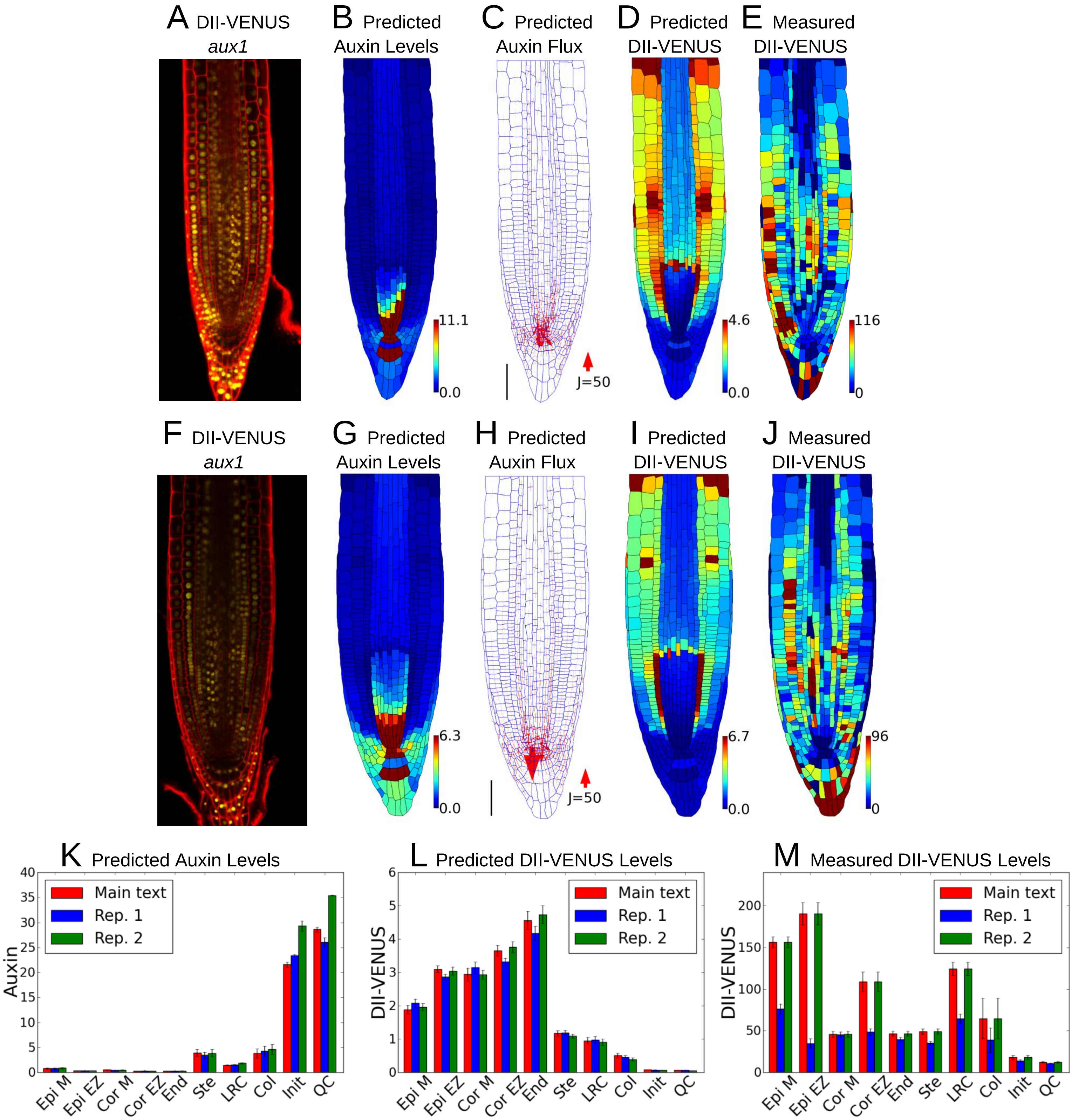

Supplemental Figure 10. Replicates of results for the *aux1* null mutant plant root. (Replicates of results shown in Figure 3, main text.)
(A-E) Replicate 1. **(F-J)** Replicate 2. **(A,F)** Confocal image showing DII-VENUS (yellow) and cell geometries (red) within the root tip (stained with propidium iodide). **(B,G)** Predicted auxin distribution. **(C,H)** Predicted auxin flux (with arrow width scaling with flux). **(D,I)** Predicted DII-VENUS distribution. **(E,J)** Measured DII-VENUS levels extracted from the confocal image in (A,F). **(K)** Mean predicted auxin concentrations in the different cell types for the three replicates. **(L)** Mean predicted DII-VENUS concentrations in the different cell types for the three replicates. **(M)** Mean measured DII-VENUS levels in the different cell types for the three replicates. Scale bars: $50\,\mu$m.

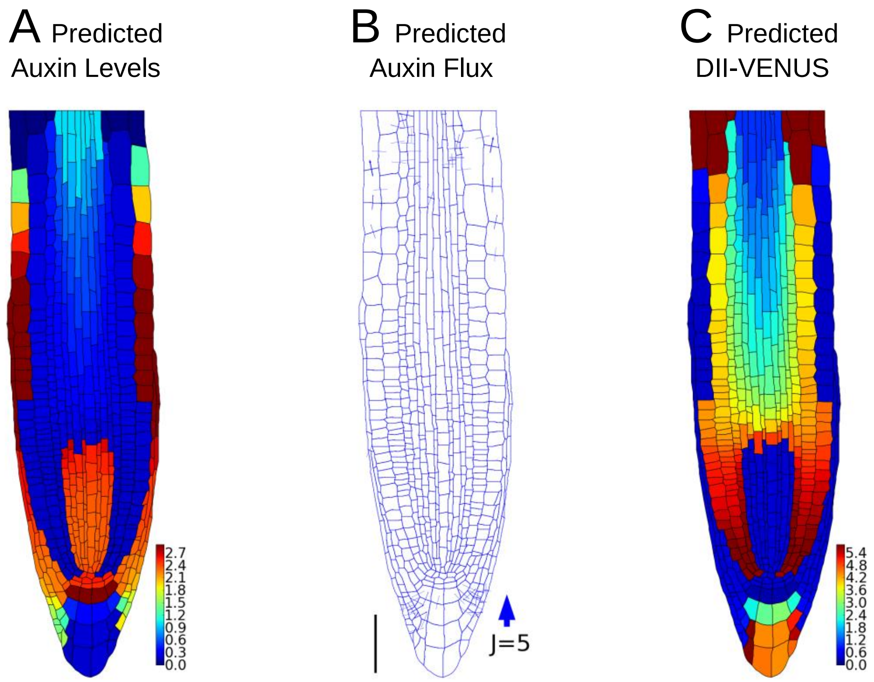

Supplemental Figure 11. Effect of omitting the polar PINs on the predicted wild-type distributions and fluxes (with auxin transport mediated by both influx and efflux carriers). (i.e. Effect of omitting the polar PINs on the results presented in Figure 2, main text.)

(A) Predicted auxin distribution.

(B) Predicted auxin flux (with arrow width scaling with flux).

(C) Predicted DII-VENUS distribution. Scale bars: 50 μm.

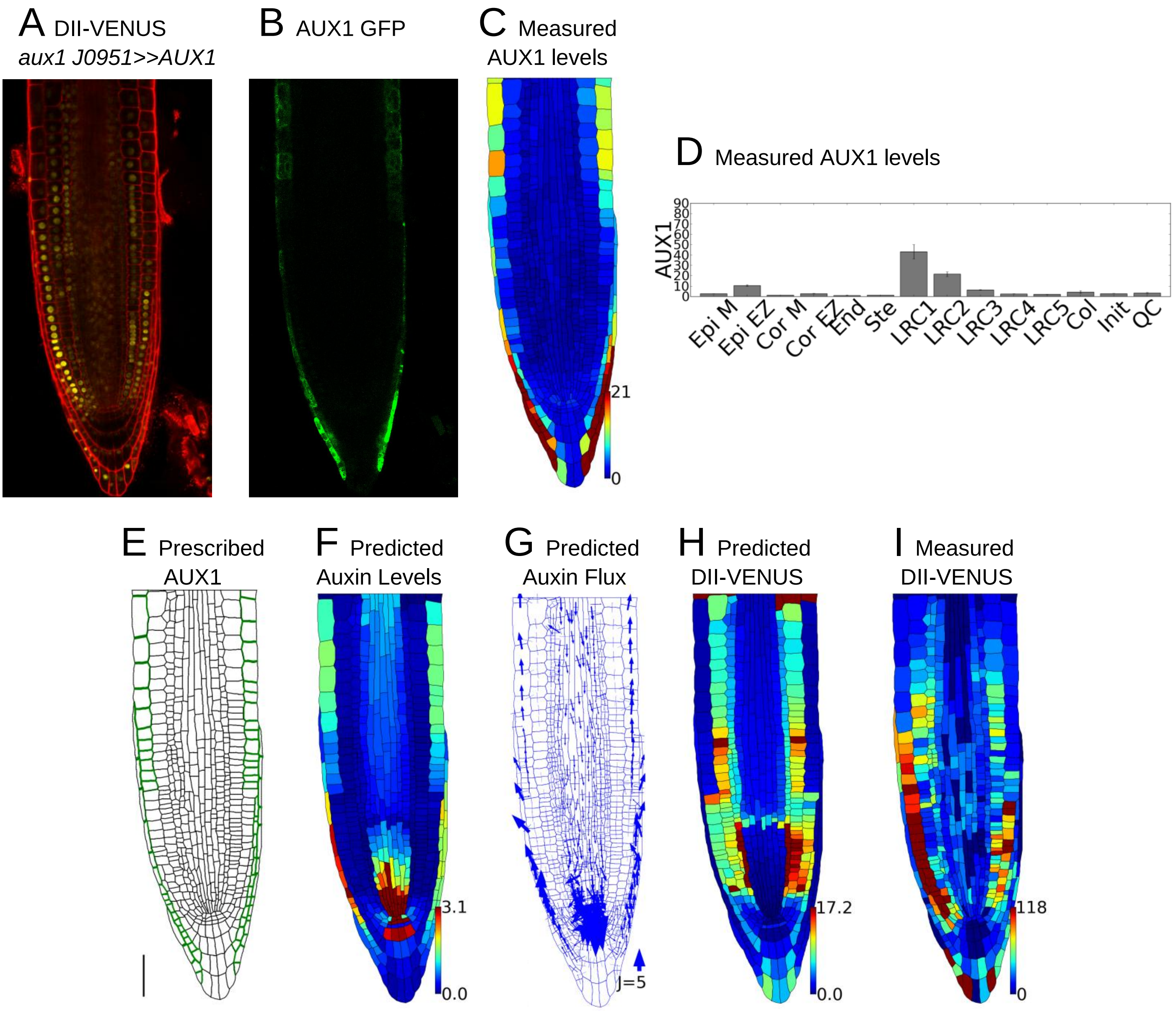

Supplemental Figure 12. Replicate 1 results for the *aux1 J0951≫AUX1* mutant plant root in which AUX1 is expressed solely in the outer LRC and epidermal cells. (Replicate of results shown in Figure 4, main text.)

(A) Confocal image of a *aux1 J0951≫AUX1* line, reporting DII-VENUS (yellow) and with propidium iodide cell-wall staining (red). **(B)** Confocal image of a *aux1 J0951≫AUX1* line, reporting AUX1 (green). **(C)** AUX1 fluorescence level for each cell extracted from confocal image in (B), heat map shows the average fluorescence calculated as the total fluorescence in the cell divided by the length of the cell's wall. **(D)** Mean AUX1 fluorescence in the different cell types. **(E)** Prescribed AUX1 distribution reflecting *aux1 J0951≫AUX1* pattern (C,D). **(F)** Predicted auxin distribution. **(G)** Predicted auxin fluxes (with arrow width scaling with flux). **(H)** Predicted DII-VENUS distribution. **(I)** Measured DII-VENUS levels extracted from the confocal image in (A). Scale bars: 50 μm.

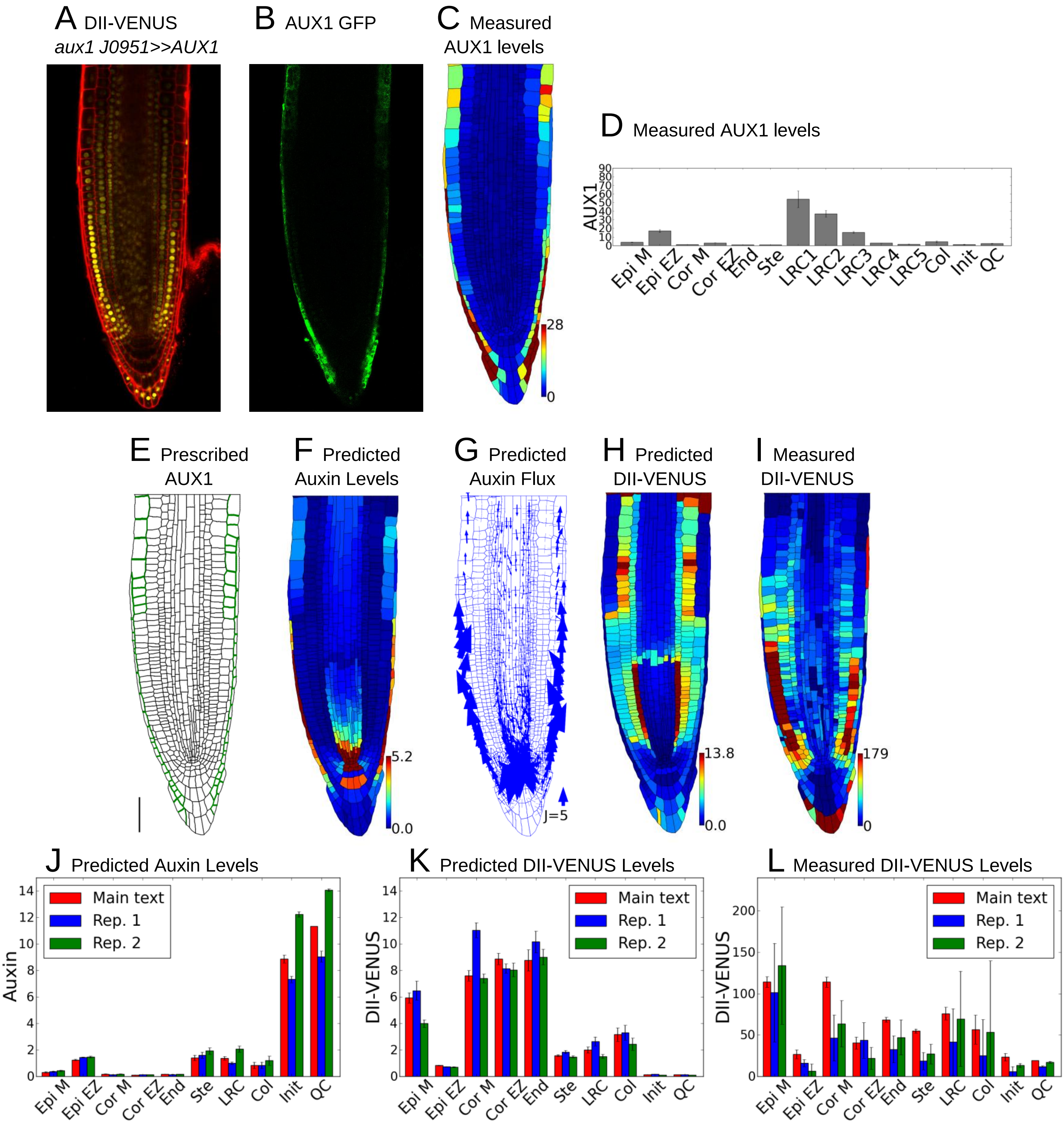

Supplemental Figure 13. Replicate 2 results for the *aux1 J0951≫AUX1* mutant plant root in which AUX1 is expressed solely in the outer LRC and epidermal cells. (Replicate of results shown in Figure 4, main text.)

Panels **(A-I)** are as in Supplemental Figure 12. **(J)** Mean predicted auxin concentrations in the different cell types for the three replicates. **(K)** Mean predicted DII-VENUS concentrations in the different cell types for the three replicates. **(L)** Mean measured DII-VENUS levels in the different cell types for the three replicates. Scale bars: 50 μm.

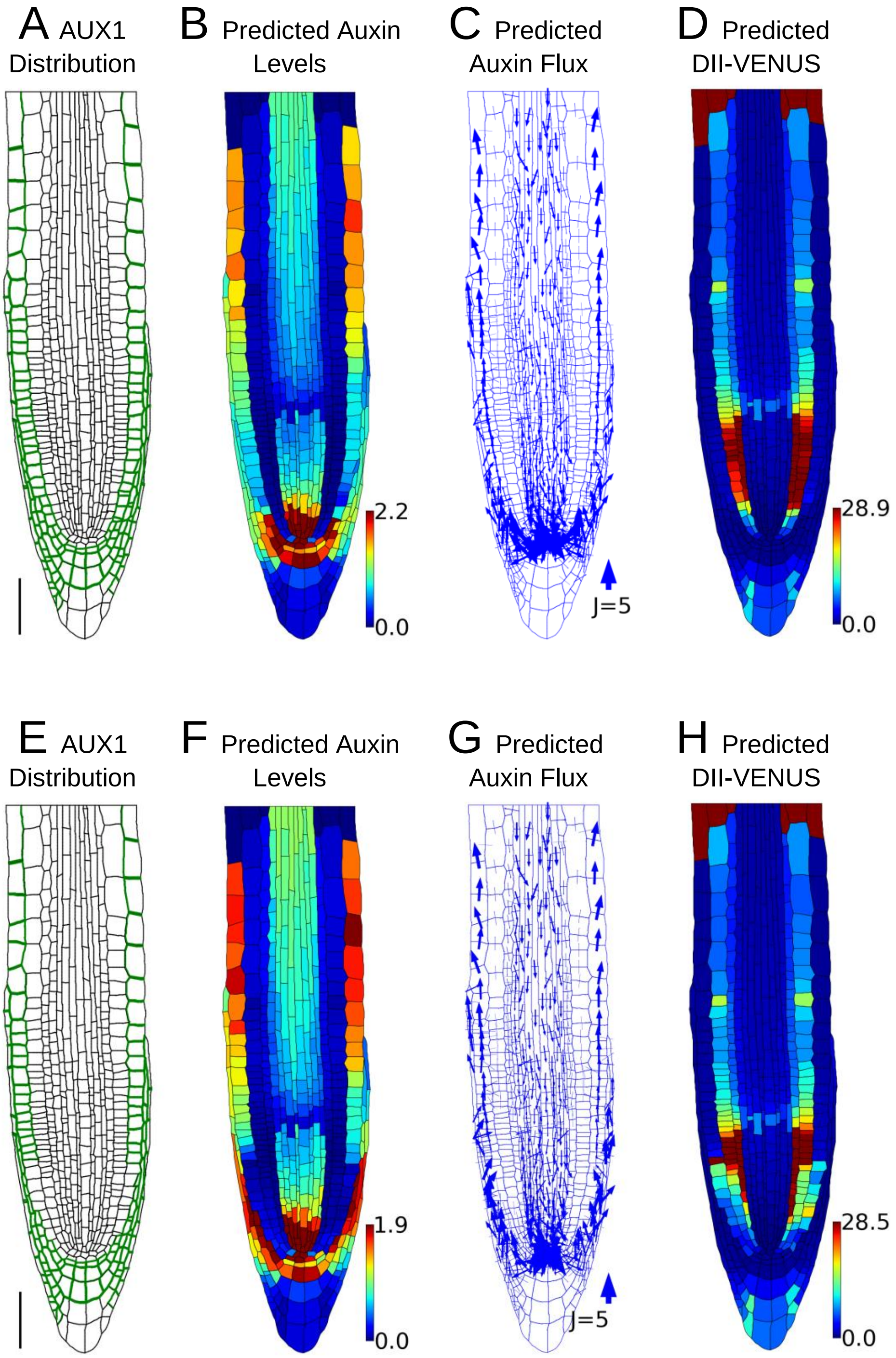

Supplemental Figure 14. Effect of AUX1 being expressed in meristematic epidermal cells on the predicted wild-type distributions and fluxes (with auxin transport mediated by both influx and efflux carriers). **(A-D)** With AUX1 on all epidermal cell membranes. **(E-H)** With AUX1 within the epidermal cells in the shootward half of the meristem. **(A,E)** Prescribed AUX1 distribution. **(B,F)** Predicted auxin distribution. **(C,G)** Predicted auxin flux (with arrow width scaling with flux). **(D,H)** Predicted DII-VENUS distribution. Scale bars: 50 μm.

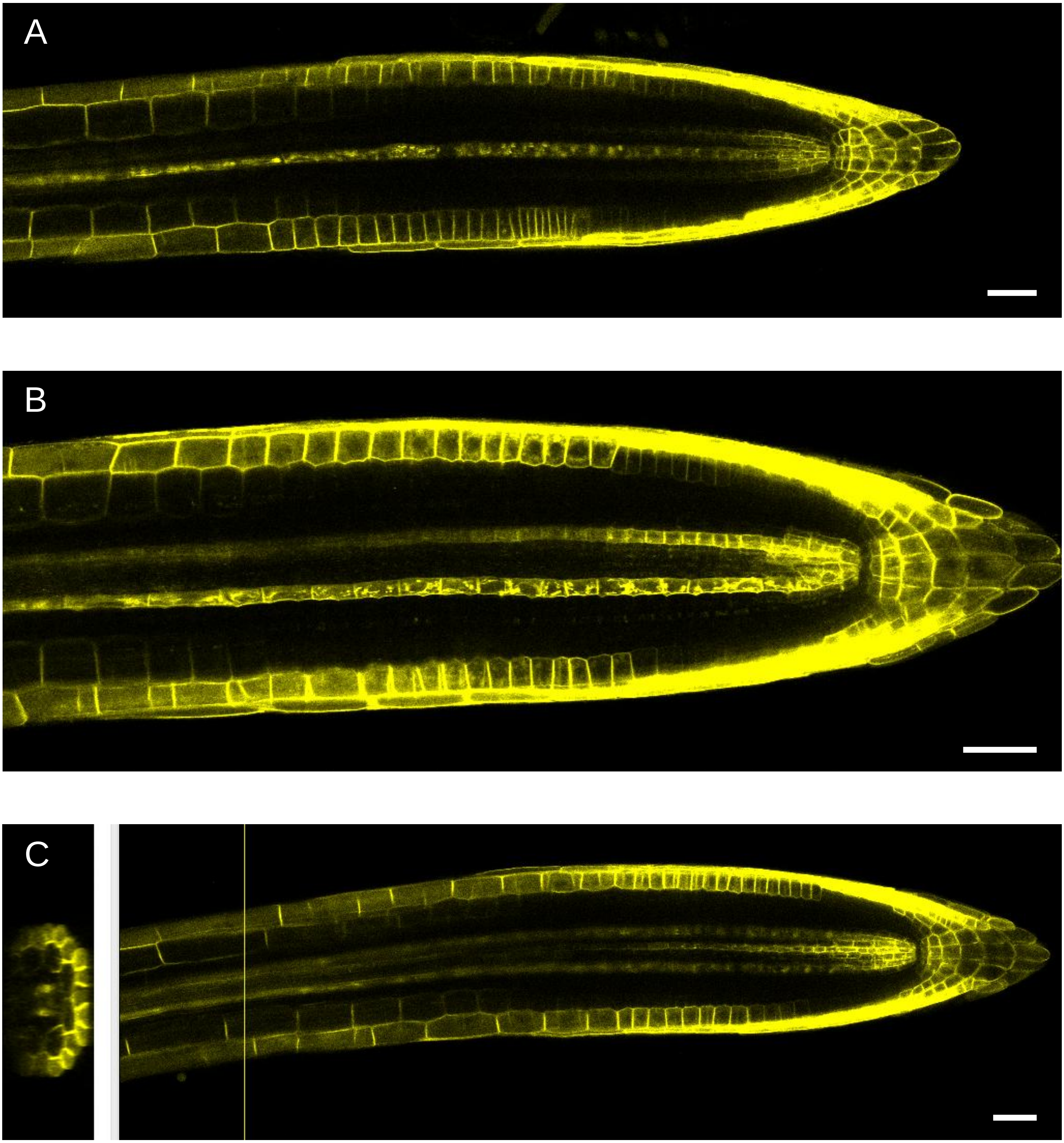

Supplemental Figure 15. Replicates for the AUX1-Ypet line. (Replicates of results shown in Figure 6A, main text.)
(A) Replicate 1. **(B)** Replicate 2 (zoom factor: 1.5). **(C)** The root imaged in Figure 6A together with orthogonal view (left panel) Position of orthogonal section marked by yellow line on right panel. Scale bars: 50 μm.

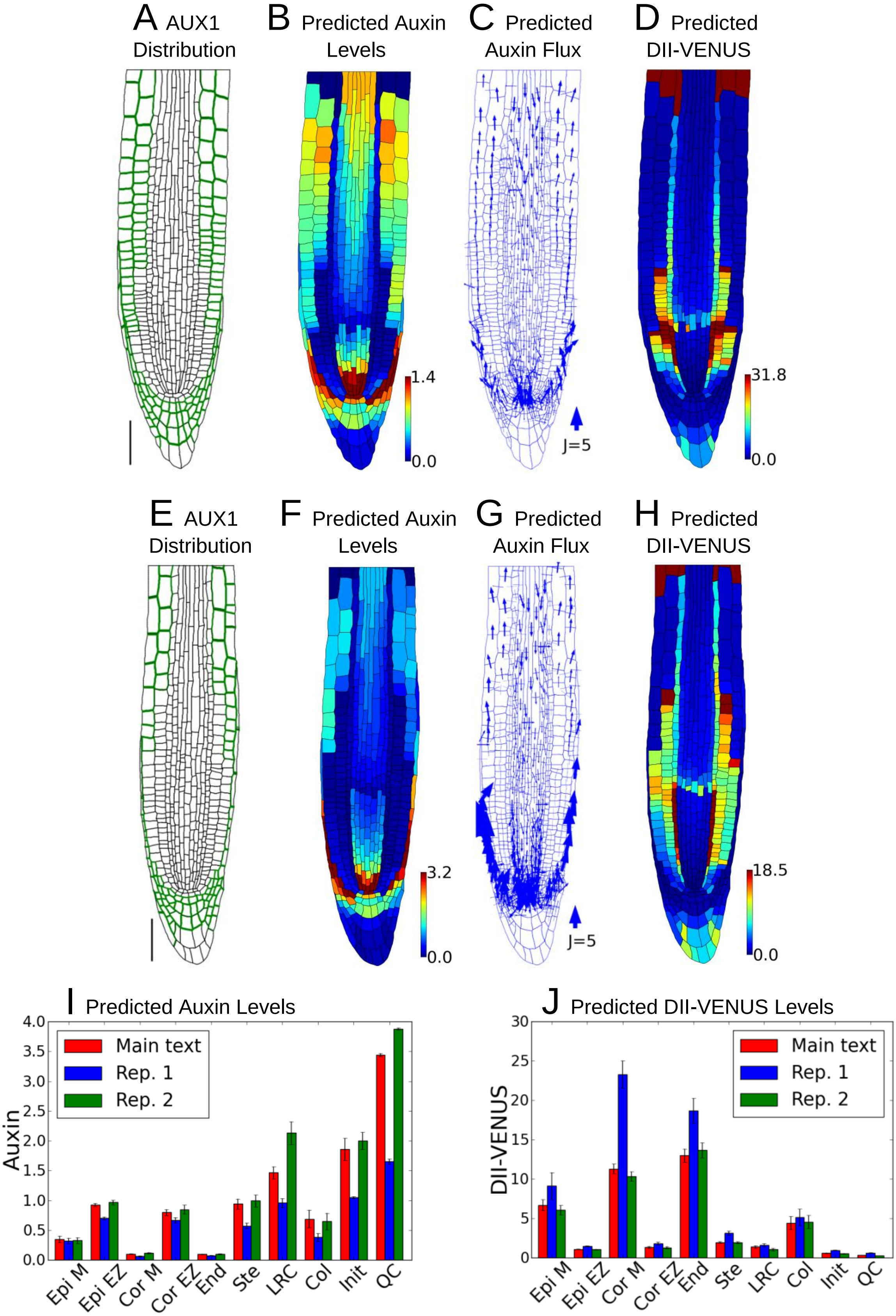

Supplemental Figure 16. Replicates of simulations for the wild-type root tip with AUX1 expressed in the elongating cortical cells. (Replicates of results shown in Figure 6B-G, main text.)
(A-D) Replicate 1. **(E-H)** Replicate 2. **(A,E)** Prescribed AUX1 distribution based on the AUX1-VENUS images. **(B,F)** Predicted auxin distribution. **(C,G)** Predicted auxin flux (with arrow width scaling with flux). **(D,H)** Predicted DII-VENUS distribution. **(I)** Mean predicted auxin concentrations in the different cell types for the three replicates. **(J)** Mean predicted DII-VENUS concentrations in the different cell types for the three replicates. Scale bars: 50 μm.

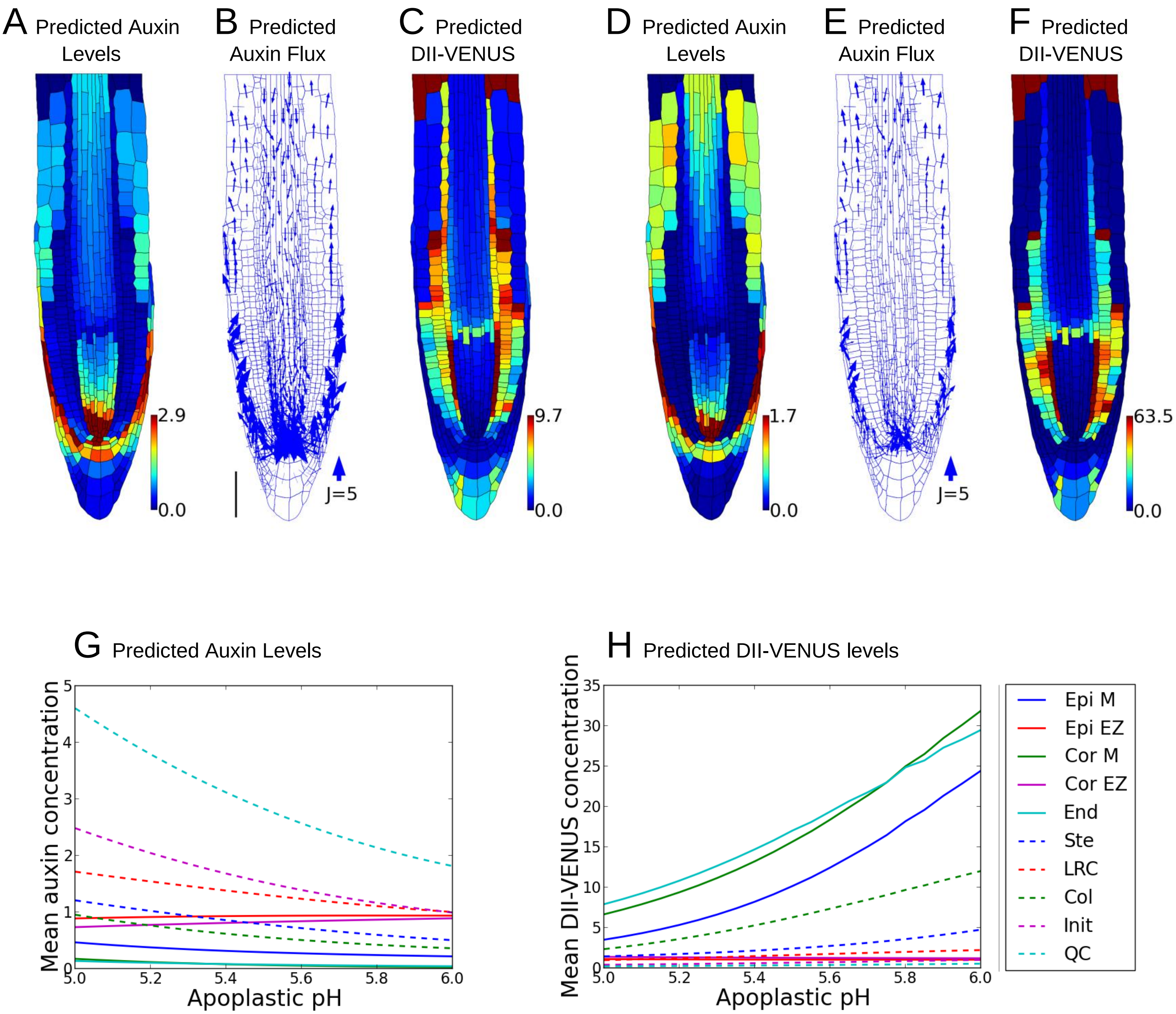

Supplemental Figure 17. Effect of apoplastic pH on the predicted distributions and fluxes in the wild-type root tip. (i.e. Effect of apoplastic pH on the results presented in Figure 6, main text.) **(A-C)** Apoplastic pH, $pH_{apo} = 5$. **(D-F)** Apoplastic pH, $pH_{apo} = 6$. **(A,D)** Predicted auxin distribution. **(B,E)** Predicted auxin flux (with arrow width scaling with flux). **(C,F)** Predicted DII-VENUS distribution. **(G)** Influence of the apoplastic pH on the mean predicted auxin concentrations in the different cell types. **(H)** Influence of the apoplastic pH on the mean predicted DII-VENUS concentrations in the different cell types. Scale bars: 50 μm.

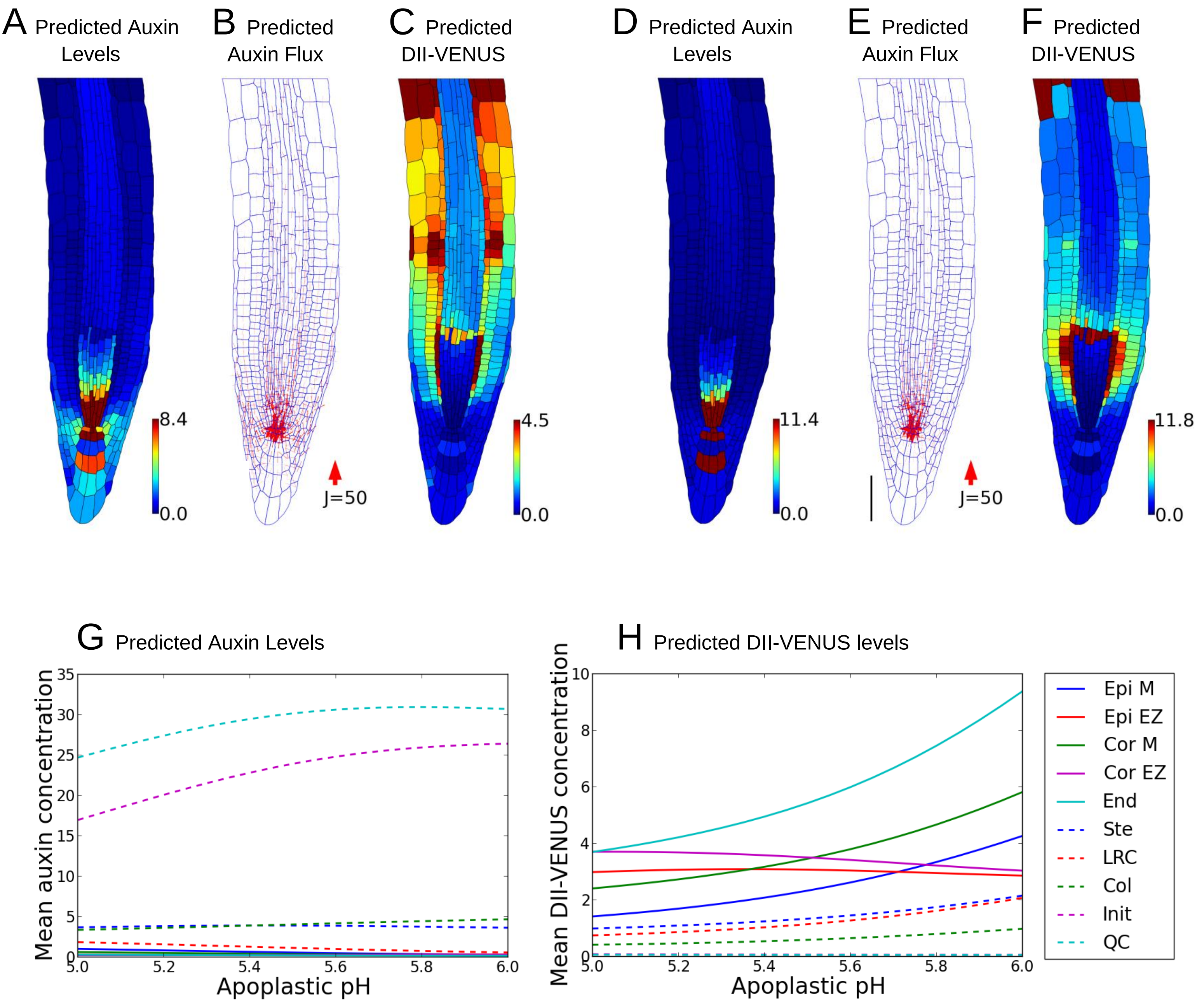

Supplemental Figure 18. Effect of apoplastic pH on the predicted distributions and fluxes in the *aux1* null mutant root tip. (i.e. Effect of apoplastic pH on the results presented in Figure 3, main text.) **(A-C)** Apoplastic pH, $pH_{apo} = 5$. **(D-F)** Apoplastic pH, $pH_{apo} = 6$. **(A,D)** Predicted auxin distribution. **(B,E)** Predicted auxin flux (with arrow width scaling with flux). **(C,F)** Predicted DII-VENUS distribution. **(G)** Influence of the apoplastic pH on the mean predicted auxin concentrations in the different cell types. **(H)** Influence of the apoplastic pH on the mean predicted DII-VENUS concentrations in the different cell types. Scale bars: 50 μm.

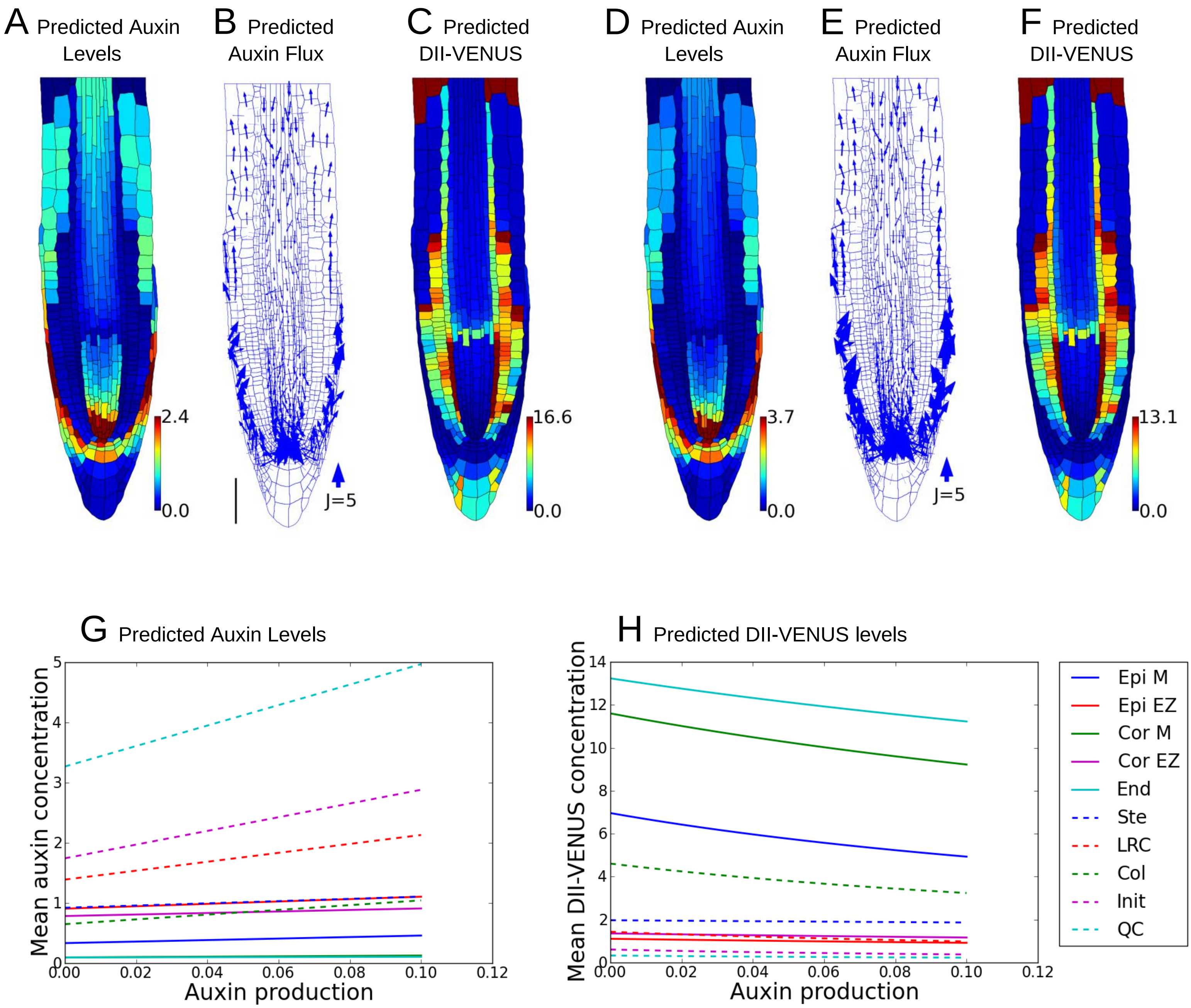

Supplemental Figure 19. Effect of auxin production in the QC and columella initials on the predicted distributions and fluxes in the wild-type root tip. (i.e. Effect of auxin production in the QC and columella initials on the results presented in Figure 6, main text.)
(A-C) Small auxin production, $\hat{\alpha}_{QC} = 0.001$. **(D-F)** Large auxin production, $\hat{\alpha}_{QC} = 0.1$. **(A,D)** Predicted auxin distribution. **(B,E)** Predicted auxin flux (with arrow width scaling with flux). **(C,F)** Predicted DII-VENUS distribution. **(G)** Influence of auxin production on the mean predicted auxin concentrations in the different cell types. **(H)** Influence of auxin production on the mean predicted DII-VENUS concentrations in the different cell types. Scale bars: 50 μm.

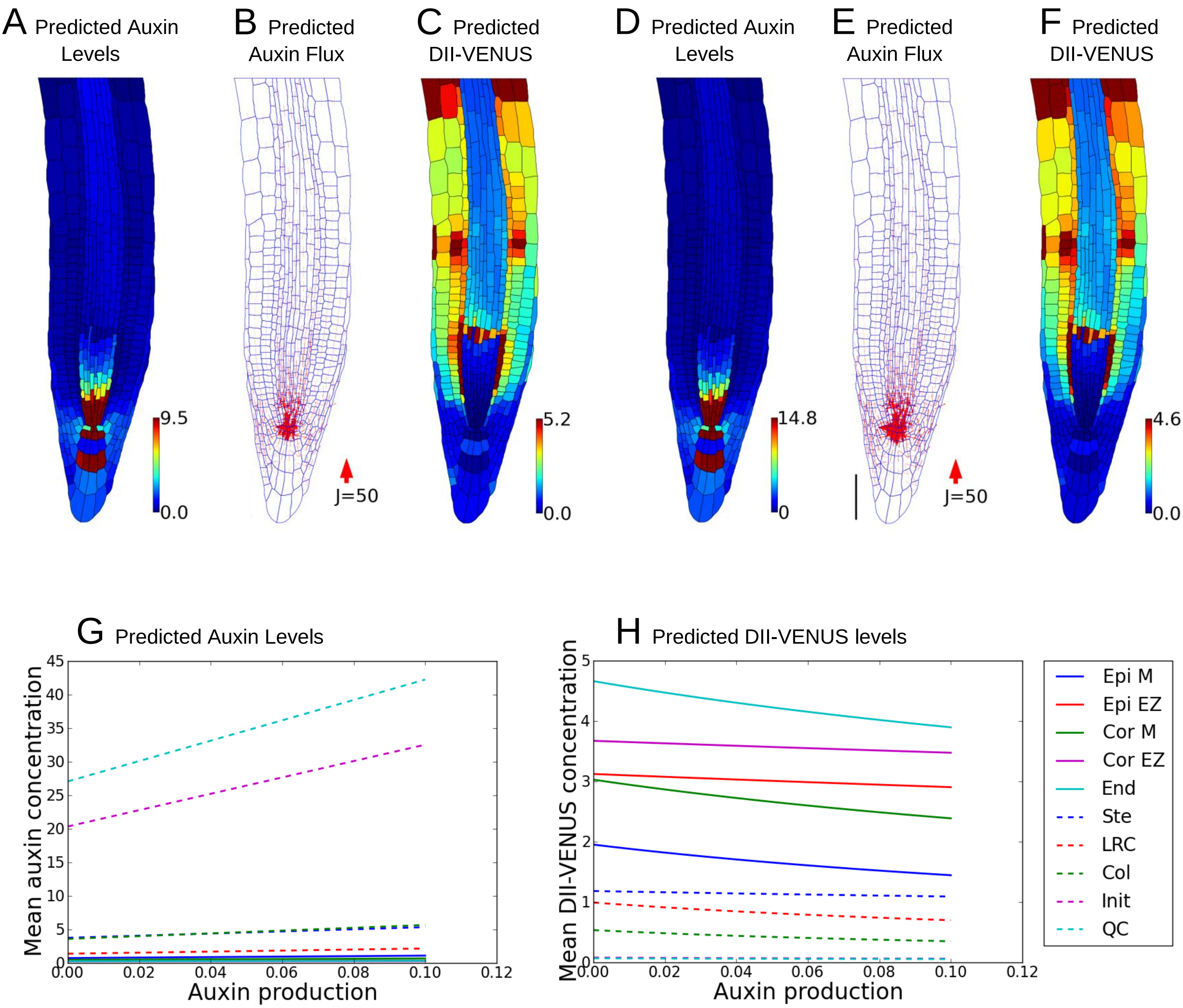

Supplemental Figure 20. Effect of auxin production in the QC and columella initials on the predicted distributions and fluxes in the *aux1* null mutant root tip. (i.e. Effect of auxin production in the QC and columella initials on the results presented in Figure 3, main text.)
(A-C) Small auxin production, $\hat{\alpha}_{QC} = 0.001$. **(D-F)** Large auxin production, $\hat{\alpha}_{QC} = 0.1$. **(A,D)** Predicted auxin distribution. **(B,E)** Predicted auxin flux (with arrow width scaling with flux). **(C,F)** Predicted DII-VENUS distribution. **(G)** Influence of the auxin production on the mean predicted auxin concentrations in the different cell types. **(H)** Influence of auxin production on the mean predicted DII-VENUS concentrations in the different cell types. Scale bars: 50 μm.

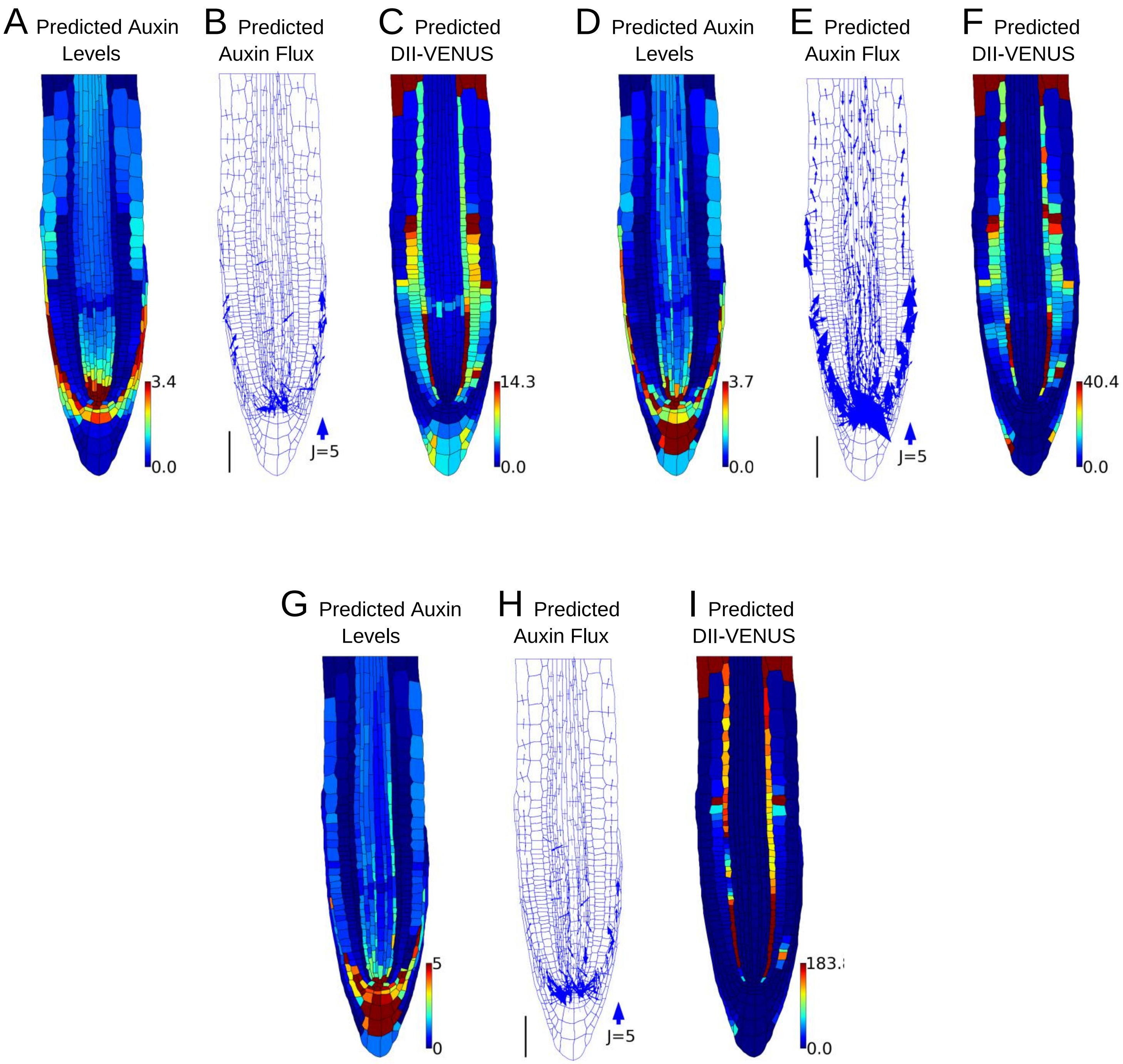

Supplemental Figure 21. Effect of omitting cell-wall diffusion and/or non-polar efflux on the predicted distributions and fluxes in a wild-type root tip (i.e. Effect of omitting cell-wall diffusion and/or non-polar efflux on the results presented in Figure 6, main text.)
(A-C) Omitting cell-wall diffusion. **(D-F)** Omitting non-polar efflux, $P_{NPE} = 0$. **(G-I)** Omitting both cell-wall diffusion and non-polar efflux. **(A,D,G)** Predicted auxin distribution. **(B,E,H)** Predicted auxin flux (with arrow width scaling with flux). **(C,F,I)** Predicted DII-VENUS distribution.

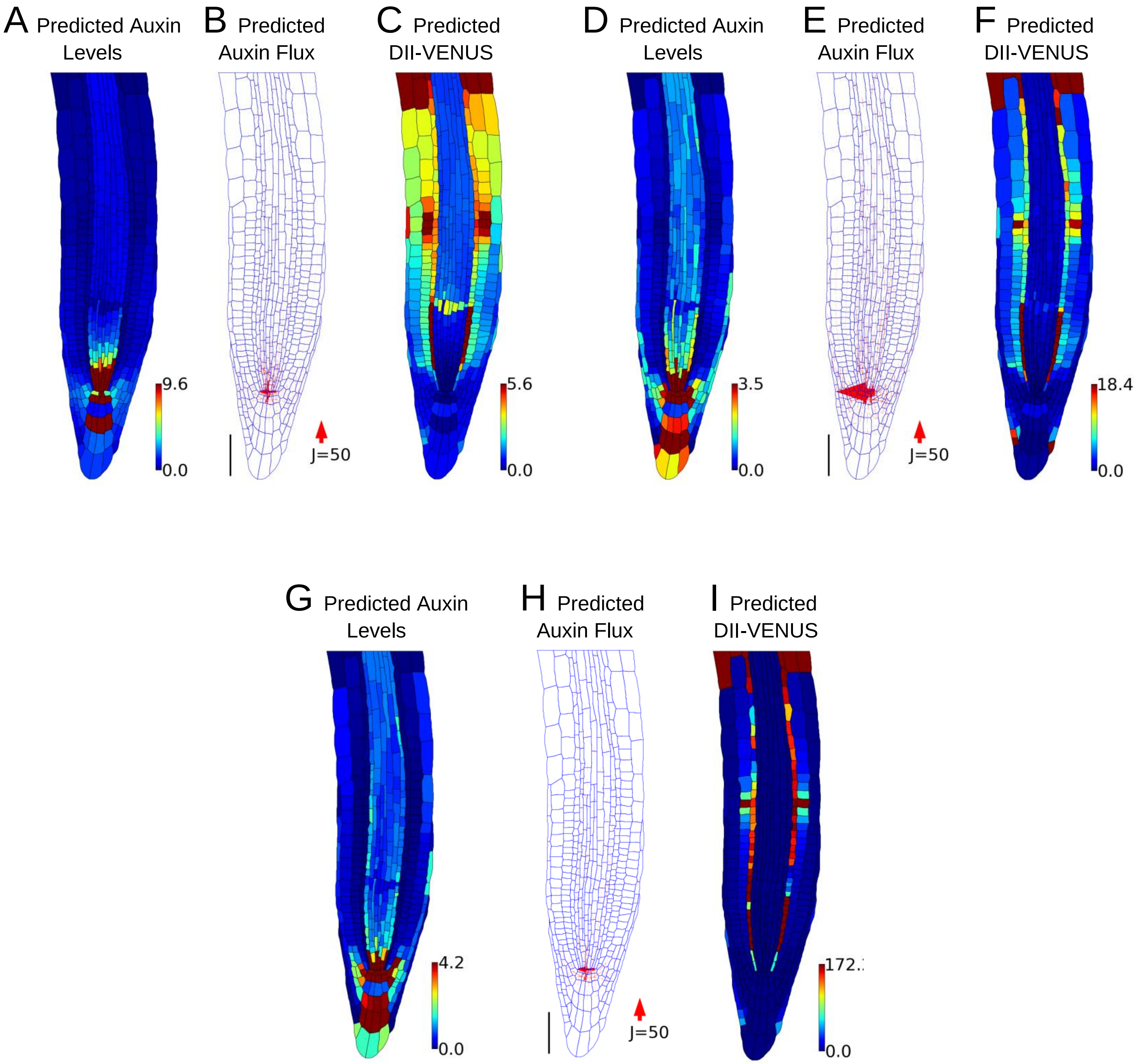

Supplemental Figure 22. Effect of omitting cell-wall diffusion and/or non-polar efflux on the predicted distributions and fluxes in an *aux1* null mutant root tip. (i.e. Effect of omitting cell-wall diffusion and/or non-polar efflux on the results presented in Figure 3, main text.)
(A-C) Omitting cell-wall diffusion. **(D-F)** Omitting non-polar efflux, $P_{NPE} = 0$. **(G-I)** Omitting both cell-wall diffusion and non-polar efflux. **(A,D,G)** Predicted auxin distribution. **(B,E,H)** Predicted auxin flux (with arrow width scaling with flux). **(C,F,I)** Predicted DII-VENUS distribution.

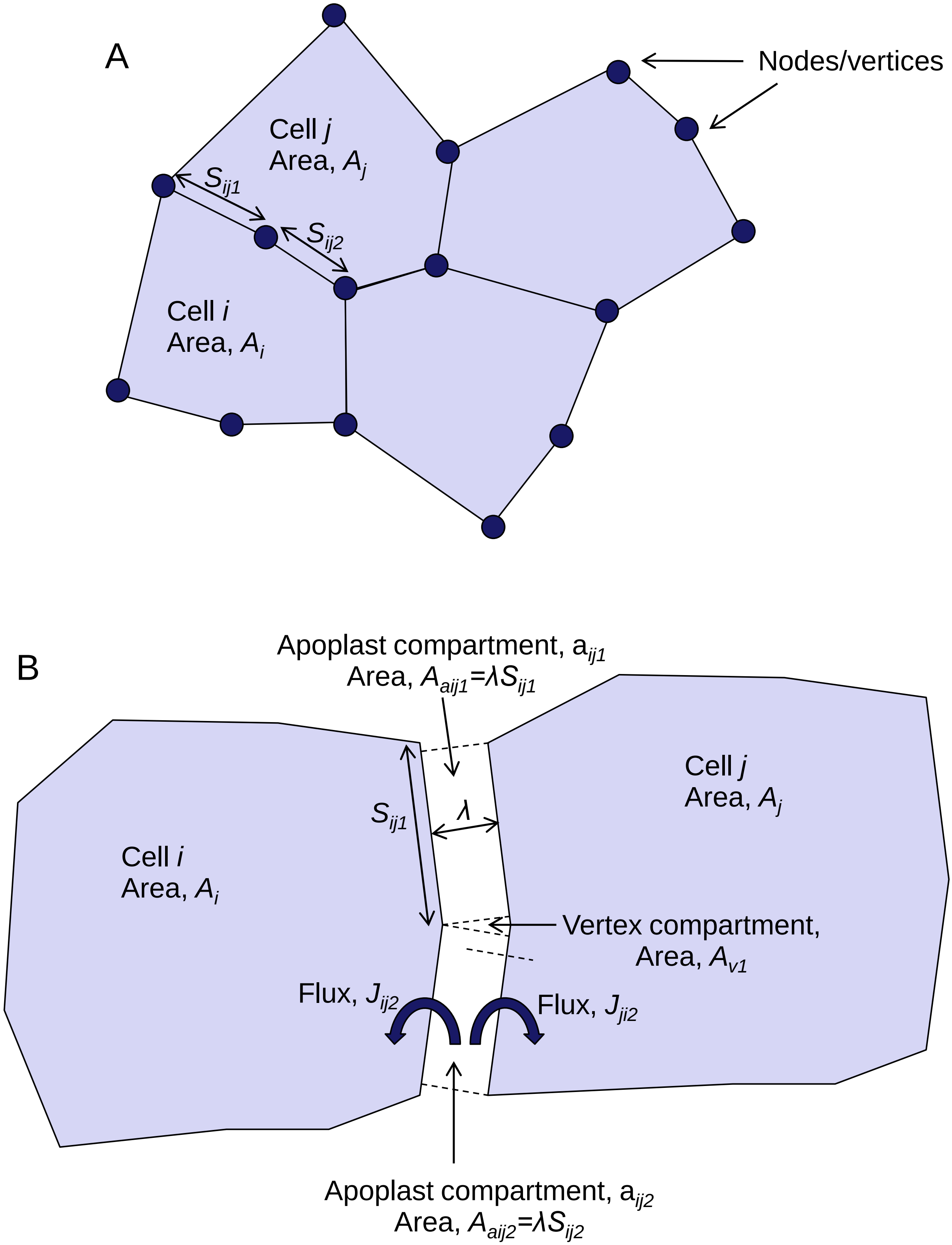

Supplemental Figure 23. Schematics illustrating the vertex-based interpretation of the multicellular plant tissues.

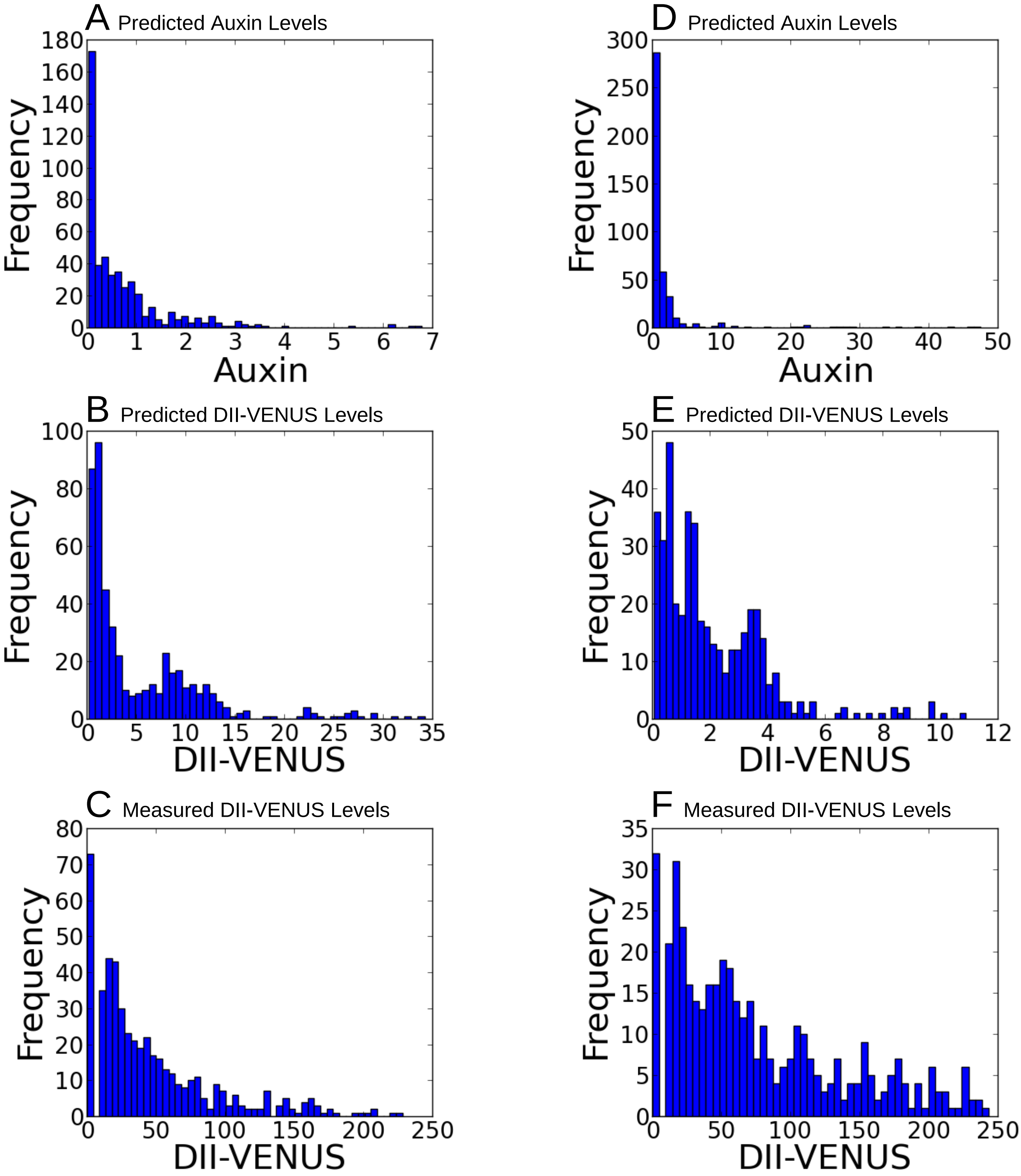

Supplemental Figure 24. Histograms showing the distributions of predicted/measured auxin and DII-VENUS levels.

(A) Predicted auxin concentrations for a wild-type root tip, corresponding to the results shown in Figure 6C, main text. **(B)** Predicted DII-VENUS concentrations for a wild-type root tip, corresponding to the results shown in Figure 6E, main text. **(C)** Measured DII-VENUS concentrations for a wild-type root tip, corresponding to the data shown in Figure 1D, main text. **(D)** Predicted auxin concentrations for an *aux1* null mutant root tip, corresponding to the results shown in Figure 3B, main text. **(E)** Predicted DII-VENUS concentrations for an *aux1* null mutant root tip, corresponding to the results shown in Figure 3D, main text. **(F)** Measured DII-VENUS concentrations for an *aux1* null mutant root tip, corresponding to the data shown in Figure 3E, main text.

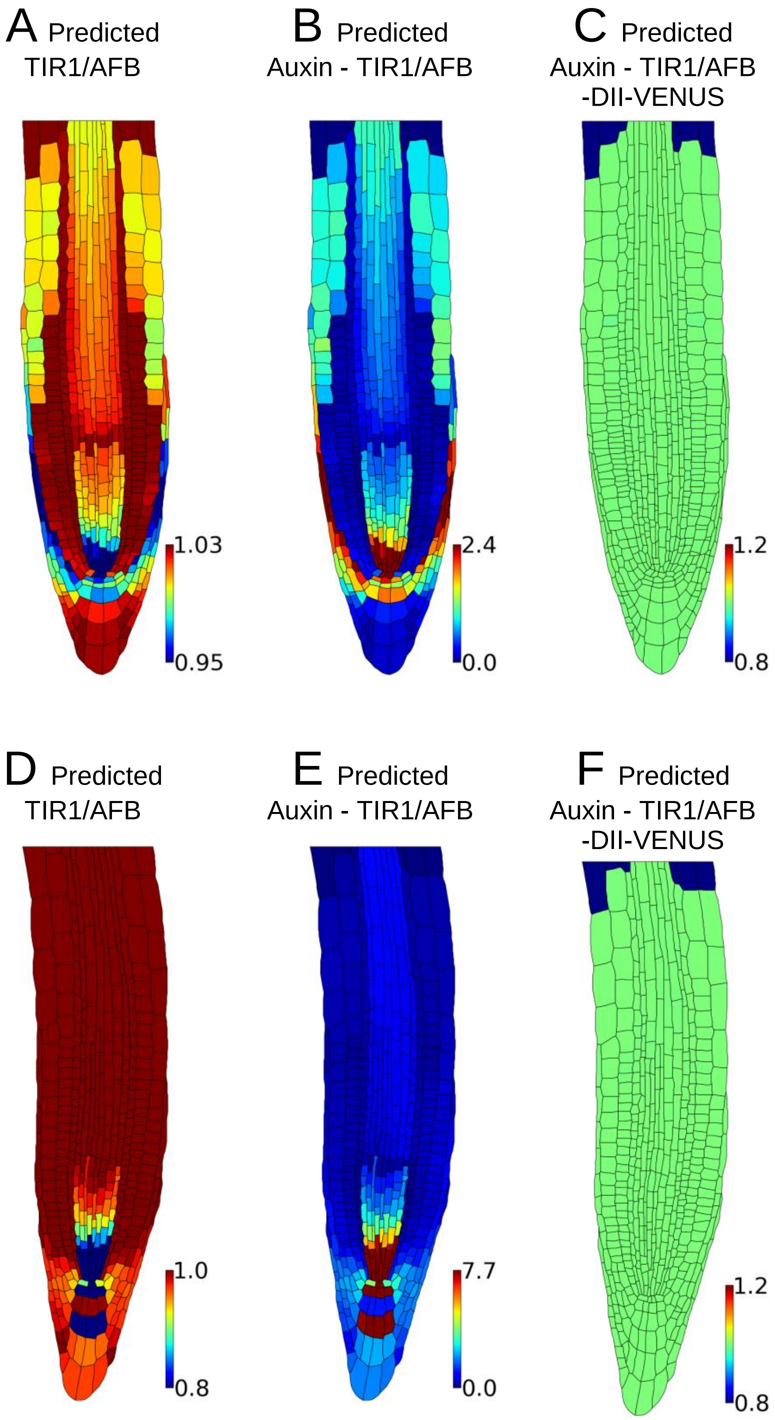

Supplemental Figure 25. Predicted distributions of the free and bound TIR1/AFB receptors. **(A-C)** Distributions for a wild-type root tip, corresponding to the results shown in Figure 6, main text. **(D-F)** Distributions for an *aux1* null mutant root tip, corresponding to the results shown in Figure 3, main text. **(A,D)** Free TIR1/AFB receptors. **(B,E)** Auxin-TIR1/AFB complexes. **(C,F)** Auxin-TIR1/AFB-DII-VENUS complexes.

Cell type	Wild type			*aux1*			*aux1 J0951≫AUX1*		
	Main text	Rep. 1	Rep. 2	Main text	Rep. 1	Rep. 2	Main	Rep. 1	Rep. 2
Epi. Meri.	47	38	47	42	48	60	75	48	57
Epi. EZ	10	23	9	8	15	7	10	13	8
Cor. Meri.	63	44	62	55	60	80	77	61	84
Cor. EZ	13	29	10	15	24	12	9	23	14
End.	79	71	73	69	79	103	80	106	107
Stele	175	140	147	149	153	172	178	160	211
LRC	72	49	54	62	67	72	80	75	81
Col.	21	16	21	16	17	19	20	20	21
Col. Init.	4	4	4	4	4	4	4	4	4
QC	2	2	2	2	2	2	1	2	2

Supplemental Table 1. Number of each cell type in each cell geometry.
The wild-type root tips are shown in Figure 1C, main text, and Supplemental Figure 4A,G.
The *aux1* null mutant root tips are shown in Figure 3A, main text, and Supplemental Figure 10A,F.
The *aux1 J0951≫AUX1* root tips (in which AUX1 is expressed solely in the outer LRC and epidermal cells) are shown in Figure 4A, main text, and Supplemental Figures 12A and 13A.

Carrier	Cell type	Region	Membrane(s)
PIN1	Stele	All	Rootward face
	Endodermis	All	Rootward and inner periclinal faces,
	Cortex	Meristem	Rootward face
PIN2	Epidermis	DMeri and EZ	Shootward face
	LRC	-	Shootward face,
	Cortex	DMeri	Rootward face
	Cortex	EZ	Shootward face
PIN3	Col initials	-	All faces
	Col, tier S1	-	All faces
	Col, tier S2	-	All faces
	Stele	All	Rootward face
PIN4	QC	-	All faces
	Col initials	-	All faces
	Col, tier S1	-	All faces
PIN7	QC	-	All faces
	Col initials	-	All faces
	Col, tier S1	-	All faces
	Col, tier S2	-	All faces
	Epidermis	PMeri	Rootward face
	Cortex	PMeri	Rootward face
	Stele	All	Rootward face
	CE initials	-	Rootward face

Supplemental Table 2. Observed distributions of different members of the PIN family, based on the images shown in Supplemental Figure 3. Here, we abbreviate the elongation zone (by EZ), distal meristem (DMeri), proximal meristem (PMeri), columella (Col) and cortical-endodermal initials (CE initials).

Cell type	Region	Member	Membrane(s)
Epidermal	PMeri	PIN7	facing a more rootward epidermal cell
		PIN7	facing a columella, QC or initial cell
	DMeri and EZ	PIN2	facing a more shootward epidermal cell
Cortical	Meristem	PIN1, PIN2, PIN7	facing a more rootward cortical cell
		PIN1, PIN7	facing a columella, QC or initial cell
	EZ	PIN2	facing a more shootward cortical cell
Endodermal	All	PIN1	facing a more rootward endodermal cell
		PIN1	facing a stele cell
		PIN1	facing a columella, QC or initial cell
Stele	All	PIN1, PIN3, PIN7	on the rootward face
LRC1	-	PIN2	facing a more shootward LRC1 cell
		PIN2	of most shootward cell which faces a more inward layer and have a central x co-ordinate less than that of the cell centre.
LRC2	-	PIN2	facing a more shootward LRC2 cell
		PIN2	of most shootward cell which faces a more inward layer and have a central x co-ordinate less than that of the cell centre.
LRC3	-	PIN2	facing a more shootward LRC3 cell
		PIN2	of most shootward cell which faces a more inward layer and have a central x co-ordinate less than that of the cell centre.
LRC4	-	PIN2	facing a more shootward LRC4 cell
		PIN2	of most shootward cell which faces a more inward layer and have a central x co-ordinate less than that of the cell centre.
LRC5	-	PIN2	facing a more shootward LRC5 cell
		PIN2	of most shootward cell which face an epidermal cell and a central x co-ordinate less than that of the cell centre.
CE initials	-	PIN7	facing a QC cell
QC	-	PIN4, PIN7	all
Col initials	-	PIN3, PIN4, PIN7	all
Col, tier S1	-	PIN3, PIN4, PIN7	all
Col, tier S2	-	PIN3, PIN7	all

Supplemental Table 3. Rules used to prescribe the PIN distribution on our virtual root geometries. Here, we abbreviate the proximal meristem (by PMeri), distal meristem (DMeri), elongation zone (EZ), lateral root cap (LRC), columella (Col) and cortical-endodermal initials (CE initials).

Parameter	Description	Value	Reference
P_{IAAH}	Passive membrane permeability	$0.56\,\mu\mathrm{m\,s}^{-1}$	Swarup *et al*, 2005
P_{AUX1}	Membrane permeability due to AUX1 influx carriers	$0.56\,\mu\mathrm{m\,s}^{-1}$	Swarup *et al*, 2005; Heisler and Jönsson, 2006
P_{LAX}	Membrane permeability due to LAX influx carriers	$0.56\,\mu\mathrm{m\,s}^{-1}$	Assumed same as AUX1
P_{PIN}	Membrane permeability due to PIN efflux carriers	$0.56\,\mu\mathrm{m\,s}^{-1}$	Swarup *et al*, 2005
P_{NPE}	Membrane permeability due to non-polar efflux carriers	$0.168\,\mu\mathrm{m\,s}^{-1}$	Assumed to be 30% of P_{PIN}
pH_c	Cytoplasmic pH	7.2	Fasano *et al*, 2001; Scott and Allen, 1999
pH_a	Apoplastic pH	5.3	Fasano *et al*, 2001
pK	Dissociation constant for auxin	4.8	Swarup *et al*, 2005
V_m	Cell membrane potential	$-0.120\,\mathrm{V}$	Sze *et al*, 1999
T	Temperature	$300\,\mathrm{K}$	Swarup *et al*, 2005
λ	Apoplast thickness	$0.14\,\mu\mathrm{m}$	Derbyshire, personal communication.
D	Diffusion coefficient within the apoplast	$3.2 \times 10^{-11}\,\mathrm{m}^2\,\mathrm{s}^{-1}$	Kramer *et al*, 2007
R	Gas constant	$8.31\,\mathrm{J\,mol}^{-1}\,\mathrm{K}^{-1}$	
F_D	Faraday's constant	$9.65 \times 10^5\,\mathrm{C\,mol}^{-1}$	

Supplemental Table 4. Parameter values used in the auxin-transport model.

Parameter	Description
k_a	Rate of association between auxin and TIR1/AFB
k_d	Rate of dissociation of the auxin-TIR1/AFB complexes
l_a	Rate of association of DII-VENUS to auxin-TIR1/AFB
l_d	Rate of dissociation of the auxin-TIR1/AFB-VENUS complexes into DII-VENUS and auxin-TIR1/AFB
l_m	Rate of dissociation of the auxin-TIR1/AFB-VENUS complexes into ubiquitinated DII-VENUS and auxin-TIR1/AFB
δ	Rate of DII-VENUS production
α	Rate of auxin production
μ	Rate of auxin degradation
$[\mathrm{TIR1}]_{\mathrm{T}}$	Total concentration of TIR1/AFB receptors

Supplemental Table 5. Description of parameters in the DII-VENUS network model (see equation (3.1) in the Supplemental Methods).

Parameter	Value
p_1^*	0.056
p_2	$0.0053\,\mathrm{min}^{-1}$
p_3^*	0.91
p_4^*	0.030
Basal auxin production rate, $\hat{\alpha}$	$0.001\,\mathrm{s}^{-1}$
Auxin production rate in QC and columella initials, $\hat{\alpha}_{QC}$	$0.01\,\mathrm{s}^{-1}$
Auxin degradation rate, β	$0.001\,\mathrm{s}^{-1}$

Supplemental Table 6. Parameters used in the reduced DII-VENUS network model, (see equation (3.11) in the Supplemental Methods). Parameters p_1^*, p_2, p_3^* and p_4^* were estimated in Band *et al*, 2012, using data from an auxin dose-response experiment (asterisks are used to label dimensionless parameters). In the QC and columella initial cells, the auxin production rate, $\hat{\alpha}$, is replaced with $\hat{\alpha}_{QC}$ in equation (3.12) in the Supplemental Methods.

Carrier	Cell type	Region	Membrane(s)
AUX1	LRC	-	all
	S1, S2 and S3	-	all
	Epidermis	EZ	all
	Epidermis	Meristem	all sides of cells with a central x-co-ordinate within 75 μm of the start of the EZ
LAX2	QC	-	all
	Columella initials	-	all
	Stele	-	all sides of cells in rootward half of meristem
LAX3	S2	-	all

Supplemental Table 7. Distributions of the AUX1/LAX influx carriers, based on the images shown in Supplemental Figure 8. Here, we abbreviate the elongation zone (by EZ).

SUPPLEMENTAL METHODS
Systems analysis of auxin transport in the Arabidopsis root apex

In this supplementary text, we provide further details of the segmentation and modeling described in the main text. The model represents a two-dimensional (2D) multicellular root geometry using data segmented from images taken with a confocal laser scanning microscope in which cell walls are stained with propidium iodide (i.e. Figure 1C, main text). We describe how these geometrical data were obtained from the images (§1), firstly, constructing a 2D plane from a confocal image stack using the newly developed SurfaceProject software (described in §1.1), and then using the CellSeT segmentation software (Pound *et al*, 2012) to characterise the cell geometries shown on the resulting 2D representation. We simulate auxin transport on these multicellular root geometries: we discuss how auxin moves between neighboring cells and apoplast compartments, and how these dynamics can be described by a system of ordinary differential equations (ODEs) (§2). The model also incorporates DII-VENUS degradation; following Band *et al*, 2012, we describe the network of interactions through which auxin degrades the DII-VENUS reporter using a system of ODEs, and show how the dynamics of this network can be simplified and coupled to the auxin-transport equations (§3). By modeling DII-VENUS, we can compare our model results with DII-VENUS intensity measurements quantified using CellSeT from the same two-dimensional plane that provided the cell geometries. The auxin-transport model depends on the prescribed distribution of the PIN, AUX1 and LAX membrane proteins. These distributions are deduced from experimental images shown in Supplemental Figures 3 and 8; we translate these observations to a set of rules which are automatically applied to our multi-cellular root geometries (§4). To produce the model results, the equations from §2 and §3 are simulated using Python (§5).

1 Characterizing the multicellular root geometries

1.1 SurfaceProject: Constructing a 2D plane from a 3D confocal image stack

Most segmentation software such as CellSeT operates on 2D image data, while confocal microscopy typically outputs a 3D image stack. In some cases it is reasonable to take a flat 2D plane through these data, represented by a single slice on the stack, before counting or measuring features projected onto this plane. Often, however, we might need to define a non-flat surface through the data, and project the 3D data onto that instead. This may be necessary where the object of interest is not lying flat *i.e.* is not lying parallel to the microscope objective. Within the plant root tip, this occurs due to the root not having a uniform diameter and due to bending; thus, different cells are in focus in different planes within the confocal stack (compare, for example, Supplemental Figures 2A,B). This provides the motivation for developing SurfaceProject.

The software works by first allowing the user to select points to include in the measuring plane from a 3D image stack in the Fiji software (Schindelin, 2008). Each user click stores a 3D (x, y, z) position, where z is the plane number in the 3D stack. Delaunay triangulation is used to convert this collection of points into a triangular mesh, with the resultant triangles defining the surface through the data that will become the target of projection (Supplemental Figure 2C,D).

Data projection itself works as follows. A new output image is created with the same height and width as the input stack, but with only one slice. For each pixel (x, y) on the output image, the triangle which encloses the point (x, y) is recovered. The location in 3D space of each point on the triangle is used to find the interpolated z-coordinate for the supplied (x, y) position, returned as a real number. The integer voxel locations on slices above and below this floating point z-coordinate are recovered, and the color data at these locations are interpolated using weights that depend on the precise float z-depth at this location. For example, if the z-position 3.75 is returned by this interpolation function, then the color information at $(x, y, \text{slice3})$ and $(x, y, \text{slice4})$ is returned, and the result averaged, with more weight ($w = 0.75$) being placed on the slice 4 color than the slice 3 color ($w = 0.25$). This procedure is repeated for each (x, y) in the output image, producing a 2D plane with interpolated data drawn from the 3D surface defined by the triangulation (Supplemental Figure 2E,F). The surface is limited, in that it cannot fold over itself (there can only be one z-coordinate for each pixel (x, y) location). This is not an issue for the application described in this paper, where precisely one color must be output for each (x, y) position.

1.2 Segmenting the root cell geometries

Images were acquired of roots stained with propidium iodide to reveal cellular organisation as detailed in Materials and Methods. We took serial optical sections about the midline of the root at 1μm intervals (taking between 24 and 35 sections per root to include all cell files in the midline). We used SurfaceProject to construct a 2D planar image from each 3D confocal image stack, and then used the CellSeT software (Pound *et al*, 2012) to segment the cell geometries. Automatic segmentation detected most of the larger cells and we corrected manually the geometries of smaller cells and less distinct regions (such as the stele). CellSeT required us to specify four parameters – we used: node spacing = 6; curvature = 1; continuity = 16; image weight = 1. Having detected the cell geometries, we identified and labeled the different cell types (as shown in Figure 1A, main text), and intensity measurements were recorded using the appropriate CellSeT plugins. The geometrical data were exported in an XML format and the nuclei (and, where applicable, membrane) intensities exported via a spreadsheet.

2 Modeling auxin dynamics within the root tip

To simulate auxin dynamics within the root tip, we use a vertex-based description of the multicellular root tip geometry. In this vertex-based tissue representation, cells have a polygonal geometry, bounded by a set of walls (i.e. line segments), each of which connects a pair of vertices. For each cell, CellSeT outputs a list of the walls bounding the cell, and a cell-type annotation (as in Figure 1A, main text). Each wall consists of one or more straight wall segments (see Supplemental Figure 23A); for each wall, CellSeT outputs the positions of the nodes that border these wall segments. Python scripts were used to import the (XML) output of CellSeT into the OpenAlea simulation environment (Pradal *et al*, 2008), which provides data structures for representing a multicellular root geometry. The cell connectivity graph, cell areas and wall lengths were precomputed to make simulations using this static geometry more efficient.

Supposing the root tip consists of N cells, we denote the cell areas by A_i for $i = 1, 2, \cdots, N$. Between two adjacent cells, i and j, we take there to be one or more apoplast compartments, corresponding to the wall segments specified by CellSeT. The areas of these apoplast compartments are denoted by $A_{aijk} \approx \lambda S_{ijk}$, where S_{ijk} denotes the length of the apoplast segment, λ is the apoplast thickness and $k = 1, 2, \cdots$ labels the one or more apoplast compartments that lie between cells i and j (see Supplemental Figure 23). (Note, $S_{ijk} = S_{jik}$ is thus the distance between two vertices or nodes.)

We simulate the auxin transport on this multicellular structure. We suppose that within each cell and apoplast compartment diffusion is sufficiently rapid that spatial variations within a compartment can be neglected. Previous authors have included non-uniform subcellular auxin distributions and modeled subcellular auxin diffusion; these effects have been particularly important for some models that sought to explain root-hair positioning (Payne and Grierson, 2009) and the distribution of auxin when the mature root is bent (Laskowski *et al*, 2008). However, whether diffusion smooths out subcellular variations depends on the cells' dimensions; a simple calculation of the relevant time scales shows that subcellular spatial variations can be considered negligible in the small cells at the root tip (Band and King, 2012). We therefore suppose auxin concentration to be homogeneous within each compartment, and denote the auxin concentration within cell i by $[\text{Auxin}]_i(t)$ and the concentration within the apoplast compartments adjacent to cells i and j by $[\text{Auxin}]_{aijk}(t)$ (noting that $[\text{Auxin}]_{aijk}(t) \equiv [\text{Auxin}]_{ajik}(t)$). As described in the main text, cell membranes can contain PIN, AUX1 and LAX proteins, which mediate the transport of anionic auxin. We denote the concentrations of PIN, AUX1 and LAX proteins on the membrane between cell i and apoplast compartment a_{ijk} by $[\text{PIN}]_{ijk}$, $[\text{AUX1}]_{ijk}$ and $[\text{LAX}]_{ijk}$ respectively (noting that, for example, $[\text{PIN}]_{ijk}$ and $[\text{PIN}]_{jik}$ represent different concentrations). For simplicity, we prescribe each of these concentrations to be either one or zero, depending on whether the carriers are or are not present on the corresponding cell membrane. The prescribed carrier distributions are based on experimental images, as described in detail in §4.

Following Swarup *et al*, 2005, the flux from apoplast compartment $aijk$ into cell i is given by

$$\begin{aligned}J_{ijk} = P_{IAAH}(A_1[\text{Auxin}]_{aijk} - B_1[\text{Auxin}]_i) &+ P_{AUX1}[\text{AUX1}]_{ijk}(A_2[\text{Auxin}]_{aijk} - B_2[\text{Auxin}]_i)\\ &+P_{LAX}[\text{LAX}]_{ijk}(A_2[\text{Auxin}]_{aijk} - B_2[\text{Auxin}]_i)\\ &+P_{PIN}[\text{PIN}]_{ijk}(A_3[\text{Auxin}]_{aijk} - B_3[\text{Auxin}]_i)\\ &+P_{NPE}(A_3[\text{Auxin}]_{aijk} - B_3[\text{Auxin}]_i),\end{aligned} \tag{2.1}$$

with

$$\begin{gathered}A_1 = \frac{1}{1+10^{pH_a-pK}}, \quad A_2 = q(\tilde{\phi})(1-A_1), \quad A_3 = q(-\tilde{\phi})(1-A_1),\\ B_1 = \frac{1}{1+10^{pH_c-pK}}, \quad B_2 = q(-\tilde{\phi})(1-B_1), \quad B_3 = q(\tilde{\phi})(1-B_1).\\ q(x) = x/(e^x-1), \quad \tilde{\phi} \equiv F_D V_m/RT,\end{gathered} \tag{2.2}$$

where P_{IAAH} is the passive membrane permeability to protonated auxin, P_{AUX1}, P_{LAX} and P_{PIN} are the effective membrane permeabilities to anionic auxin due to the AUX1, LAX and PIN carriers respectively, P_{NPE} is the effective membrane permeability to anionic auxin due to the non-polar efflux carriers (comprising the non-polar PINs and ABCBs), pH_a and pH_c are the pH of the apoplast and cell cytoplasms respectively, pK is the dissociation constant of auxin, T is the temperature, V_m is the potential difference across the cell membrane, F_D is Faraday's constant and R is the gas constant. The first term in (2.1) represents the diffusion of protonated auxin, the second the AUX1-mediated transport of anionic auxin, the third the LAX-mediated transport of anionic auxin, the fourth the PIN-mediated transport of anionic auxin and the fifth the non-polar efflux-carrier-mediated transport of anionic auxin. Details of the derivation of these flux terms can be found in Band and King, 2012.

We also simulate the auxin fluxes due to diffusion between adjacent apoplast compartments. To do this, we consider compartments at each vertex, of area A_{vl} and with auxin concentration $[\text{Auxin}]_{vl}(t)$, for $l = 1, 2, 3, \cdots$ (Supplemental Figure 23B). The diffusive flux from a vertex compartment, with label l, to an adjacent apoplast compartment, a_{ijk}, is given by

$$J_{ijkl} = \frac{2D}{S_{ijk}}([\text{Auxin}]_{vl} - [\text{Auxin}]_{aijk}), \tag{2.3}$$

where parameter D is the auxin diffusion coefficient within the apoplast and λ is the apoplast thickness. (Note that $J_{ijkl} = J_{jikl}$.)

The fluxes across the cell membranes and between adjacent apoplast compartments affect the auxin concentrations according to

$$\frac{\mathrm{d}[\text{Auxin}]_i}{\mathrm{d}t} = \frac{1}{A_i}\sum_{j\in C_i}\sum_{k=1}^{N_{ij}} S_{ijk}J_{wijk}, \tag{2.4a}$$

$$\frac{\mathrm{d}[\text{Auxin}]_{aijk}}{\mathrm{d}t} = -\frac{1}{\lambda}(J_{ijk} + J_{jik}) + \frac{1}{S_{ijk}}\sum_{m\in V_{ijk}} J_{ijkm}, \tag{2.4b}$$

$$\frac{\mathrm{d}[\text{Auxin}]_{vk}}{\mathrm{d}t} = -\frac{\lambda}{A_{vl}}\sum_{ijk\in W_l} J_{ijkl}, \tag{2.4c}$$

where C_i denotes the set of cells adjacent to cell i, N_{ij} denotes the number of apoplast compartments between cells i and j, V_{ijk} denotes the pair of vertex compartments adjacent to apoplast compartment a_{ijk} and W_l denotes the collection of apoplast compartments, a_{ijk}, adjacent to vertex l. With respect to the right-hand sides, the term in (2.4a) and the first term in (2.4b) describe the change in concentrations due to the fluxes across the cell membranes, whereas the second term in (2.4b) and the term in (2.4c) represent the fluxes between adjacent apoplast compartments.

Equations (2.4) form a system of coupled ordinary differential equations that govern the auxin concentrations within all the cells, apoplast compartments and vertex compartments. The auxin-transport model depends on fourteen parameter values; previous studies have quoted appropriate values for these parameters (given in Supplemental Table 4), and these are used in the simulations in the main text. Appendix B of Band and King, 2012, discusses these choices in detail.

Using these parameter values, we find that the fluxes across the cell membranes and the fluxes from adjacent apoplast segments make comparable contributions to the apoplast concentrations (2.4b): the rate of the fluxes across the cell membranes is of the order of P_{PIN}/λ, whereas the rate of the fluxes between adjacent apoplast compartments is of the order of D/S_{typ}^2 (where S_{typ} is the typical length of an apoplast compartment); using the parameter values in Supplemental Table 4 and $S_{typ} = 3\,\mu\text{m}$ (based on the CellSeT settings used), we find $P_{PIN}/\lambda = 2.8$ and $D/S_{typ}^2 = 3.6$. Thus, to model auxin dynamics accurately, we must simulate both membrane transport and apoplastic diffusion. To investigate the relative roles of each of these components, we also present simulations where apoplastic diffusion is neglected (Supplemental Figures 21 and 22); the derivation of the resulting equations is given in §2.1.

Considering the approximate magnitudes of the terms in (2.4a,c), we find that the fluxes across the cell membranes affect the intracellular auxin concentrations at a rate of the order of $P_{PIN}S_{typ}/A_{typ}$ where A_{typ} is the typical cell area; taking the typical cell area to equal the average cell area in the segmented wild-type root tip in Figure 1C, we have $A_{typ} = 110\,\mu\text{m}^2$, resulting in a rate of $0.015\,\text{s}^{-1}$. Supposing that $A_{vl} \approx \lambda^2$, the fluxes between apoplast compartments affect the vertex concentrations at a rate of the order of $D/(S_{typ}\lambda)$ (using (2.4c)); using the parameter estimates in Supplemental Table 4, this corresponds to a rate of $53\,\text{s}^{-1}$. Given the magnitude of the flux terms on the right-hand side of (2.4c) is significantly larger than that of the flux terms in (2.4a,b), we approximate the vertex concentrations as being quasi-steady (which increases simulation efficiency), i.e. equation (2.4c) is simplified to give

$$[\text{Auxin}]_{vl} = \frac{\sum_{ijk\in W_l} \dfrac{[\text{Auxin}]_{aijk}}{S_{ijk}}}{\sum_{ijk\in W_l} \dfrac{1}{S_{ijk}}}. \tag{2.5}$$

The expressions (2.5) are used to calculate the effective vertex concentrations; these values are then used to calculate the fluxes, (2.3), when simulating the equation for the apoplastic auxin concentrations (2.4b). We note that this quasi-steady approximation is exact for steady-state solutions. In §5, we detail how the quasi-steady approximation improves simulation efficiency and quantify its effect on the evolution to the steady solution. Based on the above order of magnitude estimates, one could also consider the apoplast concentrations to be quasi steady; however, in this case the rate of change of each cell's auxin concentration depends on the auxin concentrations in every other cell within the root geometry. As a result the Jacobian of the system of equations is no longer sparse; we expect this lack of sparsity to militate against improvements in simulation efficiency and so do not pursue this approximation here.

We represent auxin flux from the shoot by prescribing a constant auxin concentration in the stele cells at the boundary of the modeled tissue, denoting this concentration by $[\mathrm{Auxin}]_b$. In the epidermal, cortical and endodermal cells at this boundary, we prescribe the auxin concentration to be zero.

2.1 Neglecting apoplastic diffusion

As described above, our order of magnitude estimates suggest that fluxes across cell membranes and diffusion within the apoplast make similar contributions to the evolution of the auxin concentrations within the apoplast (see equation (2.4b)). To assess the relative roles of these two flux components, we also consider a simplified model in which we neglect apoplastic diffusion, in effect exploiting the fact that the apoplast is thin, $\lambda \ll 1$. In the limit as $\lambda \to 0$, equation (2.4b) shows that the wall-concentrations are quasi-steady and depend only on the fluxes across the cell membranes (the contribution of apoplastic diffusion being negligible). Thus, $J_{wij} = -J_{wji}$ and, using (2.1), we obtain

$$\begin{aligned}
[\mathrm{Auxin}]_{aijk} = \big(& (B_1 P_{IAAH} + B_2 P_{AUX1} [\mathrm{AUX1}]_{ijk} + B_2 P_{LAX} [\mathrm{LAX}]_{ijk} \\
& \qquad + B_3 P_{PIN} [\mathrm{PIN}]_{ijk} + B_3 P_{NPE}) [\mathrm{Auxin}]_i \\
& + (B_1 P_{IAAH} + B_2 P_{AUX1} [\mathrm{AUX1}]_{jik} + B_2 P_{LAX} [\mathrm{LAX}]_{jik} \\
& \qquad + B_3 P_{PIN} [\mathrm{PIN}]_{jik} + B_3 P_{NPE}) [\mathrm{Auxin}]_j \big) \\
& \times \big(2A_1 P_{IAAH} + 2A_3 P_{NPE} + A_2 P_{AUX1} ([\mathrm{AUX1}]_{ijk} + [\mathrm{AUX1}]_{jik}) \\
& \qquad + A_2 P_{LAX} ([\mathrm{LAX}]_{ijk} + [\mathrm{LAX}]_{jik}) + A_3 P_{PIN} ([\mathrm{PIN}]_{ijk} + [\mathrm{PIN}]_{jik}) \big)^{-1}.
\end{aligned} \tag{2.6}$$

The formula (2.6) can then be used to approximate the apoplast concentrations when calculating the fluxes (2.1) and solving (2.4a). The auxin-transport model is then governed by a system of N ODEs for the auxin concentrations within every cell, (2.4a); unlike in the previous approximation (2.4a,b,2.5), the rate of change of each cell's auxin concentration depends only on that of its neighbors.

3 Modeling the DII-VENUS distribution

Our experimental images show the levels of DII-VENUS, a fluorescent reporter that is rapidly degraded by auxin (Brunoud *et al*, 2012). Auxin degrades DII-VENUS via a network of interactions (shown in Supplemental Figure 1), which has recently been modeled (Band *et al*, 2012), providing a quantitative relationship between the dynamics and levels of auxin and DII-VENUS. Following Band *et al*, 2012, the DII-VENUS dynamics within each cell can be described using a system of coupled nonlinear ordinary differential equations (ODEs) for the concentrations of auxin, $[\mathrm{Auxin}]_i$, DII-VENUS, $[\mathrm{VENUS}]_i$, TIR1/AFB receptors, $[\mathrm{TIR1}]_i$, auxin-TIR1/AFB complexes, $[\mathrm{Auxin}\cdot\mathrm{TIR1}]_i$, and auxin-TIR1/AFB-DII-VENUS complexes, $[\mathrm{Auxin}\cdot\mathrm{TIR1}\cdot\mathrm{VENUS}]_i$:

$$\begin{aligned}
\frac{\mathrm{d}[\mathrm{Auxin}]_i}{\mathrm{d}t} &= k_d[\mathrm{Auxin}\cdot\mathrm{TIR1}]_i - k_a[\mathrm{Auxin}]_i[\mathrm{TIR1}]_i + \alpha - \mu[\mathrm{Auxin}]_i \\
&\qquad + \frac{1}{A_i}\sum_{j\in C_i}\sum_{k=1}^{N_{ij}} S_{ij}J_{aijk}, && (3.1\mathrm{a}) \\
\frac{\mathrm{d}[\mathrm{TIR1}]_i}{\mathrm{d}t} &= -k_a[\mathrm{Auxin}]_i\,[\mathrm{TIR1}]_i + k_d[\mathrm{Auxin}\cdot\mathrm{TIR1}]_i, && (3.1\mathrm{b}) \\
\frac{\mathrm{d}[\mathrm{Auxin}\cdot\mathrm{TIR1}]_i}{\mathrm{d}t} &= k_a[\mathrm{Auxin}]_i\,[\mathrm{TIR1}]_i - k_d[\mathrm{Auxin}\cdot\mathrm{TIR1}]_i \\
&\quad + (l_d + l_m)[\mathrm{Auxin}\cdot\mathrm{TIR1}\cdot\mathrm{VENUS}]_i \\
&\quad - l_a[\mathrm{Auxin}\cdot\mathrm{TIR1}]_i\,[\mathrm{VENUS}]_i, && (3.1\mathrm{c}) \\
\frac{\mathrm{d}[\mathrm{Auxin}\cdot\mathrm{TIR1}\cdot\mathrm{VENUS}]_i}{\mathrm{d}t} &= l_a[\mathrm{Auxin}\cdot\mathrm{TIR1}]_i\,[\mathrm{VENUS}]_i \\
&\quad - (l_d + l_m)[\mathrm{Auxin}\cdot\mathrm{TIR1}\cdot\mathrm{VENUS}]_i, && (3.1\mathrm{d}) \\
\frac{\mathrm{d}[\mathrm{VENUS}]_i}{\mathrm{d}t} &= \delta - l_a[\mathrm{VENUS}]_i\,[\mathrm{Auxin}\cdot\mathrm{TIR1}]_i \\
&\qquad + l_d[\mathrm{Auxin}\cdot\mathrm{TIR1}\cdot\mathrm{VENUS}]_i, && (3.1\mathrm{e})
\end{aligned}$$

where $i = 1, 2, \cdots, N$ labels the cells, and the final term in (3.1a) represents the change in auxin concentration due to fluxes across the cell membrane (from (2.4a)). The network model, (3.1), depends on eight parameters which are described in Supplemental Table 5. Implicit in (3.1) is the assumption that the total number of TIR1/AFB receptors is conserved in each cell. Figure S3 in Band *et al*, 2012 shows that the level of each member of the TIR1/AFB family is approximately uniform within the Arabidopsis root tip; we therefore suppose that the total concentration of TIR1/AFB receptors is the same in each cell, i.e.

$$[\mathrm{TIR1}]_i + [\mathrm{Auxin}\cdot\mathrm{TIR1}]_i + [\mathrm{Auxin}\cdot\mathrm{TIR1}\cdot\mathrm{VENUS}]_i = [\mathrm{TIR1}]_{\mathrm{T}}, \qquad (3.2)$$

for $i = 1, 2, \cdots, N$, where $[\mathrm{TIR1}]_\mathrm{T}$ denotes the total concentration of TIR1/AFB recepetors in each cell.

As described in Band *et al*, 2012, if we scale these equations and suppose that complex formation occurs rapidly, we can reduce the network model to a single equation for the DII-VENUS concentration. We summarise the derivation of this reduced model below.

At the steady state, the concentrations of each of the network components can be written in terms of the auxin concentration (using (3.1b-e, 3.2)):

$$\begin{aligned}
[\mathrm{VENUS}] &= \frac{\delta(l_d + l_m)(k_d + k_a[\mathrm{Auxin}]_i)}{l_a k_a [\mathrm{Auxin}]_i (l_m[\mathrm{TIR1}]_\mathrm{T} - \delta)}, && (3.3a)\\
[\mathrm{TIR1}] &= \frac{k_d(l_m[\mathrm{TIR1}]_\mathrm{T} - \delta)}{l_m(k_d + k_a[\mathrm{Auxin}]_i)}, && (3.3b)\\
[\mathrm{Auxin}\cdot\mathrm{TIR1}] &= \frac{k_a[\mathrm{Auxin}]_i(l_m[\mathrm{TIR1}]_\mathrm{T} - \delta)}{l_m(k_d + k_a[\mathrm{Auxin}])}, && (3.3c)\\
[\mathrm{Auxin}\cdot\mathrm{TIR1}\cdot\mathrm{VENUS}] &= \frac{\delta}{l_m}. && (3.3d)
\end{aligned}$$

Within the stele cells at the boundary of the modeled tissue, the prescribed, constant auxin concentration is $[\mathrm{Auxin}]_b$. The concentrations of the other components within these cells will evolve to their steady states, which are related to the auxin concentration, $[\mathrm{Auxin}]_b$, via (3.3); we denote these steady-state boundary cell concentrations by $[\mathrm{TIR1}]_b$, $[\mathrm{VENUS}]_b$, $[\mathrm{Auxin}\cdot\mathrm{TIR1}]_b$ and $[\mathrm{Auxin}\cdot\mathrm{TIR1}\cdot\mathrm{VENUS}]_b$.

Within each cell, we consider concentrations relative to these boundary values, scaling according to

$$\begin{gathered}
t = [\mathrm{VENUS}]_b t^*/\delta, \quad [\mathrm{Auxin}] = [\mathrm{Auxin}]_b[\mathrm{Auxin}]^*, \quad [\mathrm{VENUS}] = [\mathrm{VENUS}]_b[\mathrm{VENUS}]^*,\\
[\mathrm{TIR1}] = [\mathrm{TIR1}]_b[\mathrm{TIR1}]^*, \quad [\mathrm{Auxin}\cdot\mathrm{TIR1}] = [\mathrm{Auxin}\cdot\mathrm{TIR1}]_b[\mathrm{Auxin}\cdot\mathrm{TIR1}]^*,\\
[\mathrm{Auxin}\cdot\mathrm{TIR1}\cdot\mathrm{VENUS}] = [\mathrm{Auxin}\cdot\mathrm{TIR1}\cdot\mathrm{VENUS}]_b[\mathrm{Auxin}\cdot\mathrm{TIR1}\cdot\mathrm{VENUS}]^*, \qquad (3.4)
\end{gathered}$$

where asterisks are used to denote the dimensionless variables. It is then convenient to express the model in terms of the following eight dimensionless parameter groupings (which we also denote with asterisks):

$$\begin{gathered}
(l_d^*, l_m^*, k_d^*, \mu^*) = \frac{[\mathrm{VENUS}]_b}{\delta}(l_d, l_m, k_d, \mu), \quad k_a^* = \frac{k_a[\mathrm{TIR1}]_b[\mathrm{VENUS}]_b}{\delta},\\
l_a^* = \frac{l_a[\mathrm{VENUS}]_b^2}{\delta}, \quad \alpha^* = \frac{\alpha[\mathrm{VENUS}]_b}{\delta[\mathrm{Auxin}]_b}, \quad \eta_{AT}^* = \frac{\alpha}{[\mathrm{TIR1}]_b\mu}. \qquad (3.5)
\end{gathered}$$

Substituting (3.4) and (3.5) into (3.1), we find that the dimensionless variables are governed by

$$\begin{aligned}
\frac{\mathrm{d}[\mathrm{Auxin}]_i^*}{\mathrm{d}t^*} &= k_a^*\big([\mathrm{Auxin}\cdot\mathrm{TIR1}]_i^* - [\mathrm{Auxin}]_i^*\,[\mathrm{TIR1}]_i^*\big) + \alpha^* - \mu^*[\mathrm{Auxin}]_i^* \\
&\qquad + \frac{[\mathrm{VENUS}]_b}{\delta}\frac{1}{A_i}\sum_{j\in C_i}\sum_{k=1}^{N_{ij}} S_{ij}J_{aijk}^*, &(3.6a)\\
\frac{\mathrm{d}[\mathrm{TIR1}]_i^*}{\mathrm{d}t^*} &= k_a^*\eta_{AT}^*\big(-[\mathrm{Auxin}]_i^*\,[\mathrm{TIR1}]_i^* + [\mathrm{Auxin}\cdot\mathrm{TIR1}]_i^*\big), &(3.6b)\\
\frac{\mathrm{d}[\mathrm{Auxin}\cdot\mathrm{TIR1}]_i^*}{\mathrm{d}t^*} &= k_d^*\big([\mathrm{Auxin}]_i^*\,[\mathrm{TIR1}]_i^* - [\mathrm{Auxin}\cdot\mathrm{TIR1}]_i^*\big) \\
&\qquad + l_a^*\big([\mathrm{Auxin}\cdot\mathrm{TIR1}\cdot\mathrm{VENUS}]_i^* - [\mathrm{Auxin}\cdot\mathrm{TIR1}]_i^*\,[\mathrm{VENUS}]_i^*\big), &(3.6c)\\
\frac{\mathrm{d}[\mathrm{Auxin}\cdot\mathrm{TIR1}\cdot\mathrm{VENUS}]_i^*}{\mathrm{d}t^*} &= (l_d^*+l_m^*)\big([\mathrm{Auxin}\cdot\mathrm{TIR1}]_i^*\,[\mathrm{VENUS}]_i^* \\
&\qquad - [\mathrm{Auxin}\cdot\mathrm{TIR1}\cdot\mathrm{VENUS}]_i^*\big), &(3.6d)\\
\frac{\mathrm{d}[\mathrm{VENUS}]_i^*}{\mathrm{d}t^*} &= 1 - \frac{(l_d^*+l_m^*)}{l_m^*}[\mathrm{Auxin}\cdot\mathrm{TIR1}]_i^*\,[\mathrm{VENUS}]_i^* \\
&\qquad + \frac{l_d^*}{l_m^*}[\mathrm{Auxin}\cdot\mathrm{TIR1}\cdot\mathrm{VENUS}]_i^*, &(3.6e)
\end{aligned}$$

where $J_{aijk}^* = J_{aijk}/[\mathrm{Auxin}]_b$ is the flux written in terms of the auxin concentrations relative to the prescribed auxin concentration in the boundary cells. Conservation of the TIR1/AFB receptors, (3.2), gives

$$\begin{aligned}
[\mathrm{TIR1}]_\mathrm{T} &= [\mathrm{TIR1}]_b[\mathrm{TIR1}]_i^* + [\mathrm{Auxin}\cdot\mathrm{TIR1}]_b[\mathrm{Auxin}\cdot\mathrm{TIR1}]_i^* \\
&\qquad + [\mathrm{Auxin}\cdot\mathrm{TIR1}\cdot\mathrm{VENUS}]_b[\mathrm{Auxin}\cdot\mathrm{TIR1}\cdot\mathrm{VENUS}]_i^*. \qquad (3.7)
\end{aligned}$$

We now suppose that complex formation and dissociation occur rapidly, so that (3.6b-d) give

$$[\mathrm{Auxin}\cdot\mathrm{TIR1}]_i^* = [\mathrm{Auxin}]_i^*[\mathrm{TIR1}]_i^*, \quad [\mathrm{Auxin}\cdot\mathrm{TIR1}\cdot\mathrm{VENUS}]_i^* = [\mathrm{Auxin}]_i^*[\mathrm{TIR1}]_i^*[\mathrm{VENUS}]_i^*. \qquad (3.8)$$

Substituting (3.8) into (3.7), we obtain

$$[\mathrm{TIR1}]_i^* = \frac{1}{p_3^* + p_4^*[\mathrm{Auxin}]_i^* + p_1^*[\mathrm{Auxin}]_i^*[\mathrm{VENUS}]_i^*}, \qquad (3.9)$$

where

$$p_1^* = \frac{[\mathrm{Auxin}\cdot\mathrm{TIR1}\cdot\mathrm{VENUS}]_b}{[\mathrm{TIR1}]_\mathrm{T}}, \quad p_3^* = \frac{[\mathrm{TIR1}]_b}{[\mathrm{TIR1}]_\mathrm{T}}, \quad p_4^* = \frac{[\mathrm{Auxin}\cdot\mathrm{TIR1}]_b}{[\mathrm{TIR1}]_\mathrm{T}}. \qquad (3.10)$$

Substituting (3.8, 3.9) into (3.6e) and returning to dimensional time (3.4), we obtain

$$\frac{\mathrm{d}[\mathrm{VENUS}]_i^*}{\mathrm{d}t} = p_2\left(1 - \frac{[\mathrm{Auxin}]_i^*[\mathrm{VENUS}]_i^*}{p_3^* + p_4^*[\mathrm{Auxin}]_i^* + p_1^*[\mathrm{Auxin}]_i^*[\mathrm{VENUS}]_i^*}\right), \tag{3.11}$$

where $p_2 = \delta/[\mathrm{VENUS}]_b$. The ODEs (3.11) are coupled to ODEs for the intracellular auxin concentrations:

$$\frac{\mathrm{d}[\mathrm{Auxin}]_i^*}{\mathrm{d}t} = \hat{\alpha} - \mu[\mathrm{Auxin}]_i^* + \frac{1}{A_i}\sum_{j\in C_i}\sum_{k=1}^{N_{ij}} S_{ij}J_{aijk}^*, \tag{3.12}$$

(where $\hat{\alpha} = \alpha/[\mathrm{Auxin}]_b$), ODEs for the auxin concentrations within the apoplast segments (2.4b), and expressions for the auxin concentrations at the vertices, (2.5). The concentrations of TIR1/AFB and TIR1/AFB complexes within each cell can then be calculated via (3.8, 3.9).

In Band *et al*, 2012, we considered the DII-VENUS degradation dynamics in a single cell and derived an equivalent reduced model in which the auxin concentration was assumed to be constant. (Setting $[\mathrm{Auxin}]_i^* = \alpha_{trj}^*$ and $p_3^*/\alpha_{trj}^* + p_4^* = q_j^*$ in (3.11), we obtain the DII-VENUS equation in Figure 2D of Band *et al*, 2012 assuming negligible photobleaching, $\lambda = 0$.) The parameters in this model were estimated by comparing model predictions with experimental measurements of the change in DII-VENUS abundance after a dose of auxin was added to the root's media. Supposing that the prescribed auxin concentration in the boundary cells represents the typical auxin concentration within the root tissue prior to the auxin dose, we also use these estimated parameters here. These parameter estimates are summarized in Supplemental Table 6. As far as we are aware, the rates of auxin production and degradation have not been accurately measured, and we use small values of $0.01\,\mathrm{s}^{-1}$ in the QC and columella initials and $0.001\,\mathrm{s}^{-1}$ in all remaining cells.

4 Specifying the carrier distributions

Simulating auxin transport within the multicellular root geometry required us to specify accurate distributions of the influx and efflux carriers on the cell membranes. Data shown in Supplemental Figures 3 and 8 were used to develop a list of rules to specify the positions of the AUX1/LAX influx carriers and PIN efflux carriers.

Cells containing an influx carrier (AUX1, LAX2 and LAX3) were observed to have the influx carrier on all sides of the cell membrane in most cell types (Supplemental Figure 8); therefore, the influx-carrier distributions can be specified simply using the information about the type and position of each cell (Figure 1A, main text). As summarized in Supplemental Table 7, we observed AUX1 to be present in the lateral root cap (LRC), elongating epidermal cells and S1, S2 and S3 tiers of the columella (Supplemental Figure 8A), LAX2 to be present in QC, columella initials and young stele tissues (Supplemental Figure 8B) and LAX3 to be present in only the S2 tier of the columella (Supplemental Figure 8C). LAX3 is also observed in the stele (Supplemental Figure 8C); however, LAX3 in these cells does not appear to be on the plasma membrane (Swarup *et al*, 2008; Péret *et al*, 2012) and no function has yet been reported for LAX3 expression in the stele; it is therefore likely that they are inactive and hence, stele LAX3 can be excluded from the model. In the epidermis, we observed AUX1 in the cells that have emerged from the LRC and the final few shootward cells that are still under the LRC (Supplemental Figure 8A). To capture this in our model, we took the position of the start of the elongation zone, labeled x_{EZ} to be the x co-ordinate of the centroid of the most shootward LRC cell (where the x-axis lies along the axis of the root, with x increasing in a shootward direction). We prescribed AUX1 to be present in the elongation-zone epidermal cells and within the meristematic epidermal cells which have a centroid with an x co-ordinate within $75\,\mu$m of x_{EZ}. AUX1 and LAX2 are also present within specific vasculature cell files within the stele (Supplemental Figure 8A,B); however, given that the asymmetric arrangement of the xylem and phloem cannot be represented in a two-dimensional model of a longitudinal root cross-section, we cannot capture accurately the auxin transport within the stele, and therefore neglect the presence of AUX1 and LAX2 within cell files of this tissue.

The model took into account the five key PIN efflux carriers present within the root: PIN1, PIN2, PIN3, PIN4 and PIN7. PIN proteins typically have polar locations, being present mainly in specific membrane domains; we observed members of the PIN family on specific cell membranes within different tissues (Supplemental Figure 3) and summarize our observations in Supplemental Table 2. In contrast to previous suggestions (Grieneisen *et al*, 2007), we did not observe PIN2 expression in the $2-5$ epidermal and cortical cells closest to the QC, consistent with the reports of Müller *et al*, 1998. PIN7 appears to be within these epidermal and cortical cells on their rootward sides, and we therefore considered two different meristematic regions: the proximal meristem, with rootward epidermal PINs, and the distal meristem, with shootward epidermal PINs. We took the boundary between the proximal and distal meristem to be the x co-ordinate $40\,\mu$m from that of the center of the wall separating the two QC cells. The remaining rules for the PIN distribution are consistent with previous literature (Abas *et al*, 2006; Blilou *et al*, 2005; Friml *et al*, 2002a;

Friml *et al*, 2002b; Müller *et al*, 1998; Peer *et al*, 2004).

Given that the relative rates of auxin transport facilitated by the different PIN proteins is unknown, the model does not distinguish the different members of the PIN family. We avoided complications by supposing that, membrane faces that contain PIN proteins have the same PIN efflux permeability. Since we used actual cell geometries, prescribing the PIN distribution using terms such as 'the shootward membrane' would have been ambiguous; therefore, where possible, the PIN distribution was defined in terms of the cell type of the neighboring cell (for example, prescribing the PINs to be on the epidermal cell membranes facing a more rootward epidermal cell). We note that, for convenience when prescribing the PIN distributions, we prescribed each layer of the LRC to be a different cell type, observing a maximum of five layers on the root geometries segmented (denoting the layers LRC1 - LRC5, where LRC1 is the outermost layer, see Figure 1A, main text).

The rules for the distributions of AUX1, LAX2, LAX3 and PIN are sumarised in Supplemental Tables 3 and 7. For a given root geometry, these rules were used to prescribe distributions of PIN, AUX1, LAX2 and LAX3 automatically (see, for example, Figures 1E and 2A, main text).

5 Simulation implementation

The simulation results shown in the main text are steady-state solutions of the system of differential equations (2.4b, 2.5, 3.11, 3.12). These steady states are obtained by numerical approximation of the solution to an initial value problem for large time. We used initial conditions in which all concentrations are equal to zero, except for the auxin concentration in the stele cells at the boundary of the modeled tissue: as auxin concentrations are normalized to this value, the auxin concentration in these cells is set to one (representing the supply of auxin from the shoot). Simulations were run until time $t = 2 \times 10^6$ seconds, at which time the concentrations in all cells had approximately reached a steady state.

The simulations were performed in the Python programming language, using the ODE solver LSODES from the ODEPACK suite (Hindmarsh, 1983) to approximate numerically solutions of the system of differential equations. This solver exploits the sparsity of the Jacobian of the system of equations; we supplied the sparsity pattern of the Jacobian to the numerical solver to improve the speed of the simulations.

As described in §2 above, we present simulations in which we have taken the auxin concentrations within the vertex compartments to be quasi-steady. With this quasi-steady approximation, simulating the results shown in Figure 6, for example, takes approximately 2330 seconds on a desktop computer, whereas the equivalent simulations without this approximation takes approximately 7300 seconds. The maximum relative difference between the predicted auxin concentrations is 0.019 at $t = 2 \times 10^6$ (the time point at which we take the distributions to have reached their steady state). We infer that the quasi-steady approximation significantly reduces simulation time and has a negligible effect on our predictions.

We present the simulation results using the Python library matplotlib (Hunter, 2007). Plotting the steady-state concentration distributions required us to choose a range for the heat map, which we prescribed automatically to minimize subjectivity. Plotting histograms of the predicted and measured concentrations of the different cells (for example, Supplemental Figure 24), we observed that the lower limit of the concentration distribution is (unsurprisingly) zero for both auxin and DII-VENUS and that the distributions are negatively skewed. The predicted and measured DII-VENUS levels show qualitatively similar distributions, providing further evidence of the accuracy of our model. Although we could have chosen the upper limit of the heat-map range to be maximum predicted/measured concentration in each case, outliers in the concentration distribution would significantly affect the appearance of the presented distribution. We therefore prescribed the heat-map upper limit to be the 95th percentile of the concentration values. We also summarize the predicted/measured auxin and DII-VENUS distributions by presenting the mean and standard error of the concentrations within the different cell types (see, for example, Figures 1I-K, 2E,F, 6F,G); the number of cells of each type in each geometry is given in Supplemental Table 1.

In the main text and supplemental figures, we present our predicted distributions of auxin and DII-VENUS. The model also predicted the concentration distribution of the free and bound TIR1/AFB receptors (equations (3.8, 3.9)); in Supplemental Figure 25, we show sample predictions of these that correspond to the simulations in Figures 3 and 6, main text. As discussed in Band *et al*, 2012, the estimates of the parameters governing the network dynamics suggest that over 90% of the TIR1/AFB receptors are unbound in a typical cell (see Supplemental Table 6). Consistent with this, we predicted only small variations in the levels of unbound TIR1/AFB receptors (Supplemental Figure 25A,D). As one would expect, we predicted that cells with high auxin concentrations have more auxin bound to the TIR1/AFB receptors, resulting in the distribution of auxin-TIR1/AFB complexes mirroring the auxin distribution (Supplemental Figure 25B,E), whereas the distribution of free TIR1/AFB receptors is the opposite (Supplemental Figure 25A,D). We predicted the concentration of auxin-TIR1/AFB-VENUS complexes to be the same in each cell (Supplemental Figure 25C,F): since we use the limit in which complex formation occurs rapidly, (3.8), the DII-VENUS concentrations are only at their steady state if the (scaled) auxin-TIR1/AFB-VENUS complex concentration equals one (see equation (3.6e)).

To characterize the model behavior fully, we must consider both concentration and flux distributions. In simulations where we include apoplastic diffusion, the fluxes across adjacent cell membranes need not be equal; to display an approximation of the magnitude of flux from cell j to cell i, we calculate the average of the fluxes across each membrane for each apoplast compartment between the two cells: $(J^*_{wijk} - J^*_{wjik})/2$. If there is more than one apoplast compartment between cells i and j, we present the sum the resulting flux contributions, weighting these with the compartments' lengths:

$$\text{Approximate } J^*_{ij} = \frac{\sum_{k=1}^{N_{ij}} \left(S_{ijk}(J^*_{wijk} - J^*_{wjik})/2 \right)}{\sum_{k=1}^{N_{ij}} S_{ijk}}. \tag{5.1}$$

Where we neglect apoplastic diffusion, the magnitudes of the fluxes across adjacent cell membranes are equal, so that the flux from cell i to cell j is simply given by $J^*_{wjik} = -J^*_{wijk}$, and we present

$$\text{Approximate } J^*_{ij} = \frac{\sum_{k=1}^{N_{ij}} (S_{ijk} J^*_{wijk})}{\sum_{k=1}^{N_{ij}} S_{ijk}}. \tag{5.2}$$

In the flux figures, we display the fluxes using arrows across cell-to-cell boundaries provided the magnitude of the flux is greater than $0.1\,\mu\text{m}\,\text{s}^{-1}$. The width of the arrows scales with the magnitude of the fluxes; to visualise the fluxes in this way, different scales are appropriate for each figure, and we display a sample arrow size in each case.

References

Abas, L., Benjamins, R., Malenica, N., Paciorek, T., Wiśniewska, J., Moulinier-Anzola, JC., Sieberer, T., Friml, J., and Luschnig, C. (2006). Intracellular trafficking and proteolysis of the Arabidopsis auxin-efflux facilitator PIN2 are involved in root gravitropism. Nat. Cell Biol. **8:** 249-256.

Band, L.R., Wells, D.M., Larrieu, A., Sun, J., Middleton, A., French, A., Brunoud, G., Mendocilla Sato, E., Wilson, M., Péret, B., Oliva, M., Swarup, R., Sairanen, I., Parry, G., Ljung, K., Beeckman, T., Garibaldi, J. M., Estelle, M., Owen, M., Vissenberg, K., Hodgman, T.C., Pridmore, T., King, J., Vernoux, T., and Bennett M.J. (2012). Root gravitropism is regulated by a transient lateral auxin gradient controlled by a tipping-point mechanism. Proc. Natl Acad. Sci. USA **109:** 4668-4673.

Band, L.R. and King, J.R. (2012). Multiscale modelling of auxin transport in the plant-root elongation zone. J. Math. Biol. **65:** 743-785.

Blilou, I., Xu, J., Wildwater, M., Willemsen, V., Paponov, I., Friml, J., Heidstra, R., Aida, M., Palme, K., and Scheres, B. (2005). The PIN auxin efflux facilitator network controls growth and patterning in Arabidopsis roots. Nature **433:** 39-44.

Brunoud, G., Wells, D.M., Oliva, M., Larrieu, A., Mirabet, V., Burrow, A.H., Beeckman, T., Kepinski, S., Traas, J., Bennett, M.J., and Vernoux, T. (2012). A novel Aux/IAA-based sensor provides a high-resolution spatio-temporal map of auxin response and distribution during plant development. Nature **482:** 103-106.

Fasano, J.M., Swanson, S.J., Blancaor, E.B., Dowd, P.E., Kao, T.H., and Gilroy, S. (2001). Changes in root cap pH are required for the gravity response of the Arabidopsis root. Plant Cell **13:** 907-921.

Friml, J., Wiśniewska, J., Benková, E., Mendgen, K., and Palme, K. (2002a). Lateral redistribution of auxin efflux regulator PIN3 mediates tropism in Arabidopsis. Nature **415:** 806-809.

Friml, J., Benková, E., Blilou, I., Wiśniewska, J., Hamann, T., Ljung, K., Woody, S., Sandberg, G., Scheres, B., Jrgens, G., and Palme, K. (2002b). AtPIN4 mediates sink-driven auxin gradients and root patterning in Arabidopsis. Cell **108:** 661-673.

Grieneisen, V.A., Xu, J., Marée, A.F., Hogeweg, P., and Scheres, B. (2007). Auxin transport is sufficient to generate a maximum and gradient guiding root growth. Nature **449:** 1008-1013.

Heisler, M. and Jönsson, H. (2006). Modeling auxin transport and plant development. J. Plant Growth Regul. **25:** 302-312.

Hindmarsh, A.C. (1983). ODEPACK, A Systematized Collection of ODE Solvers, in Scientific Computing, eds R. S. Stepleman et al. (North-Holland, Amsterdam), pp 55-64.

Hunter, J.D. (2007). Matplotlib: A 2D graphics environment. Comput. Sci. Eng. **9:** 90-95.

Kramer, E.M., Frazer, N.L., and Baskin, T.I. (2007). Measurement of diffusion within the cell wall in living roots of Arabidopsis thaliana. J. Exp. Bot. **58:** 30053015.

Laskowski, M., Grieneisen, V.A., Hofhuis, H., Hove, C.A.T., Hogeweg, P., Marée, A.F.M., and Scheres, B. (2008). Root system architecture from coupling cell shape to auxin transport. PLoS Biol. **6:** e307

Müller, A., Guan, C., Gälweiler, L., Tnzler, P., Huijser, P., Marchant, A., Parry, G., Bennett, M., Wisman, E., and Palme, K. (1998). AtPIN2 defines a locus of Arabidopsis for root gravitropism control. EMBO Journal **17:** 6903-6911.

Payne, R.J.H. and Grierson, C.S. (2009). A theoretical model for ROP localisation by auxin in Arabidopsis root hair cells. PLoS ONE **4:** e8337.

Peer, W.A., Bandyopadhyay, A., Blakeslee, J.J., Makam, S.N., Chen, R.J., Masson, P.H., and Murphy, A.S. (2004). Variation in expression and protein localization of the PIN family of auxin efflux facilitator proteins in flavonoid mutants with altered auxin transport in Arabidopsis thaliana. Plant Cell **16:** 18981911.

Péret, B., Swarup, K., Ferguson, A., Seth, M., Yang, Y., Dhondt, S., James, N., Casimiro, I., Perry, P., Syed, A., Yang, H., Reemmer, J., Venison, E., Howells, C., Perez-Amador, M.A., Yun, J., Alonso, J., Beemster, G.T., Laplaze, L., Murphy, A., Bennett, M.J., Nielsen, E., and Swarup R. (2012). AUX/LAX genes encode a family of auxin influx transporters that perform distinct functions during Arabidopsis development. Plant Cell **24:** 2874-2885.

Pound, M.P., French, A.P., Wells, D.M., Bennett. M.J., and Pridmore T. (2012). CellSeT: novel software to extract and analyze structured networks of plant cells from confocal images. Plant Cell **24:** 1353-1361.

Pradal, C., Dufour-Kowalski, S., Boudon, F., Fournier, C., and Godin, C. (2008). OpenAlea: A visual programming and component-based software platform for plant modeling. Funct. Plant Biol. **35:** 751-760.

Scott, A.C. and Allen, N.S. (1999). Changes in cytosolic pH within Arabidopsis root columella cells play a key role in the early signaling pathway for root gravitropism. Plant Physiol. **121:** 1291-1298.

Schindelin, J., Arganda-Carreras, I., Frise, E., Kaynig, V., Longair, M., Pietzsch, T., Preibisch, S., Rueden, C., Saalfeld, S., Schmid, B., Tinevez, J.Y., White, D.J., Hartenstein, V., Eliceiri, K., Tomancak, P., and Cardona, A. (2012). Fiji: an open-source platform for biological-image analysis. Nat. Methods **9:** 676-682.

Swarup, K., Benkova, E., Swarup, R., Casimiro, I., Peret, B., Yang, Y., Parry, G., Nielsen, E., De Smet, I., Vanneste, S., Levesque, M.P., Carrier, D., James, N., Calvo, V., Ljung. K., Kramer, E., Roberts, R., Graham, N., Marillonnet, S., Patel, K., Jones, J.D., Taylor, C.G., Schachtman, D.P., May, S., Sandberg, G., Benfey, P., Friml, J., Kerr, I., Beeckman, T., Laplaze, L., and Bennett, M.J. (2008). The auxin inux carrier LAX3 promotes lateral root emergence. Nat. Cell Biol. **10:** 946-954.

Swarup, R., Kramer, E.M., Perry, P., Knox, K., Leyser, H.M., Haseloff, J., Beemster, G.T., Bhalerao, R., and Bennett, M.J. (2005). Root gravitropism requires lateral root cap and epidermal cells for transport and response to a mobile auxin signal. Nat. Cell Biol. **7:** 1057-1065.

Sze, H., Li, X., and Palmgren, M. (1999). Energization of plant cell membranes by H+ pumping ATPases: regulation and biosynthesis. Plant Cell **11:** 677-689.